A generalized computational model for the simulation of adsorption packed bed reactors - Parametric study of five reactor geometries for cooling applications

Giorgos Papakokkinos*, Jesús Castro, Joan López, Assensi Oliva*

Heat and Mass Transfer Technological Center (CTTC) Universitat Politècnica de Catalunya-BarcelonaTech (UPC)
ESEIAAT, Colom 11, E-08222 Terrassa, Barcelona, Spain

Abstract

Environmental concerns regarding global warming and ozone depletion urge towards sustainable solutions for satisfying the increasing cooling demand. Adsorption cooling technology could form part of the solution since it can be driven by solar energy and industrial or vehicular waste heat, as well as it employs non ozone-destructive refrigerants. However, its low performance hinders its extensive development and commercialization. The design of the adsorption reactor is crucial for its performance improvement, since its inherent cyclic operation imposes a compromise between the Specific Cooling Power and the Coefficient of Performance. A generalized three-dimensional computational model based on unstructured meshes is presented, capable to simulate all potential geometries. Dynamic conjugate simulations of the packed bed and the heat exchanger allow to study the latter's influence on the reactor performance. A parametric study of five reactor geometries was conducted, demonstrating quantitatively the strong impact of the solid volume fraction, fin length and fin thickness on the performance. Within the studied range, the Specific Cooling Power is maximized for the highest solid volume fraction and for the lowest fin thickness and fin length. The effect of the adsorbed mass spatial distribution on the desorption phase is discussed. A sensitivity analysis exhibits the importance of the heat transfer coefficient between the two domains. Copper and aluminium are compared as heat exchanger materials, revealing that the former performs more effectively, although the difference is appreciable only for longer fin lengths. The presented numerical model can be employed for improving the design of adsorption packed bed reactors.

Keywords: Adsorption cooling, Adsorption packed bed reactor, Numerical simulation, Geometric analysis, Silica-gel/water

---

*Corresponding author

Email addresses: `giorgos@cttc.upc.edu` (Giorgos Papakokkinos), `cttc@cttc.upc.edu` (Assensi Oliva)

Nomenclature

Latin characters

A area $[\text{m}^2]$

c_p specific heat capacity $[\text{J kg}^{-1}\,\text{K}^{-1}]$

d_p particle diameter [m]

D_s effective diffusivity $[\text{m}^2\,\text{s}^{-1}]$

D_0 reference diffusivity $[\text{m}^2\,\text{s}^{-1}]$

E_a activation energy $[\text{J kg}^{-1}]$

h_if heat transfer coefficient at the interface between packed bed and heat exchanger $[\text{W m}^{-2}\,\text{K}^{-1}]$

h_pi adsorbent-adsorbate convective heat transfer coefficient $[\text{W m}^{-2}\,\text{K}^{-1}]$

K_0 Tóth pre-exponential constant $[\text{kg}_\text{w}\,\text{kg}_\text{s}^{-1}\,\text{Pa}^{-1}]$

K_D permeability $[\text{m}^2]$

K_E inertia-related parameter for Ergun equation $[\text{m}^2]$

M mass [kg]

Nu   Nusselt number [-]

$\mathbf{n}$ surface normal vector

P pressure [Pa]

Pr   Prandtl number [-]

$\dot{Q}$ heat flux [W]

q_m Tóth monolayer capacity $[\text{kg}_\text{w}\,\text{kg}_\text{s}^{-1}]$

R universal gas constant $[\text{J mol}^{-1}\,\text{K}^{-1}]$

R_g gas constant $[\text{J kg}^{-1}\,\text{K}^{-1}]$

Re   Reynolds number [-]

T temperature [K]

t time [s]

$\vec{u}$ velocity vector $[\text{m s}^{-1}]$

w adsorption capacity $[\text{kg}_\text{w}\,\text{kg}_\text{s}^{-1}]$

w^* adsorption equilibrium capacity $[\text{kg}_\text{w}\,\text{kg}_\text{s}^{-1}]$

Greek characters

α	specific exchange surface area per unit volume for spherical particles [m^{-1}]
β	geometry-specific parameter [m or °]
γ	fin length [m]
δ	fin thickness [m]
ΔH_{ads}	isosteric enthalpy of adsorption [J kg^{-1}]
ΔH_{evap}	latent heat of evaporation [J kg^{-1}]
ϵ	void fraction [-]
λ	thermal conductivity [W m^{-1} K^{-1}]
μ	dynamic viscosity [Pa s]
ρ	density [kg m^{-3}]
σ	standard deviation
τ	Tóth dimensionless constant [-]
ϕ	angle [°]

Subscripts

aver	average
Al	aluminium
b	bed
Cu	copper
evap	evaporator
f	control face
g	gas
hx	heat exchanger
init	initial
inst	instantaneous
if	interface between heat exchanger and packed bed
l	liquid
p	particle
pi	particle interface
rel	relative
s	solid
t	total
w	water

Abbreviations

COP   Coefficient of Performance

CV   control volume

GEOM   geometry

HTF   heat transfer fluid

SCP   Specific Cooling Capacity $[\mathrm{W\,kg^{-1}}]$

SVF   Solid Volume Fraction [%]

1. Introduction

The cooling demand is expected to increase as a result of the human population growth and socioeconomic development [1], the elevated temperatures due to global warming [2], as well as the urban heat island effect [2] provoked by the ongoing urbanization of Earth [3]. Satisfying this demand is conflictive with the fossil fuel finiteness and the urgency to reduce greenhouse gases emissions in order to mitigate the global warming phenomenon [4]. Furthermore, a paradigm shift should take place in accordance to the Montreal protocol [5], with respect to the elimination of the ozone-destructive refrigerants.

The adsorption cooling technology could contribute to a sustainable solution for these environmental concerns, since it can be driven by solar energy, industrial or vehicular waste heat, as well as it employs non ozone-destructive refrigerants.

Despite the environmental benefits of adsorption cooling systems, their low performance hinders their commercialization and widespread development [6]. Researches for improving their performance focus mainly on (i) the adsorption properties of the materials involved [7], (ii) the configuration and operational characteristics of the thermodynamic cooling cycles [8] and (iii) the design of the adsorption reactors [9]. This study is dedicated to the latter and specifically to the design of adsorption packed bed reactors.

The inherent cyclic operation of adsorption reactors imposes a challenging task regarding their design, which aims for the optimum compromise between the Specific Cooling Power (SCP) and the Coefficient of Performance (COP). The shape and size of the heat exchanger - the solid mass between the heat transfer fluid (HTF) and the packed bed - play a crucial role in the performance of the system.

On the one hand, increasing the size of the heat exchanger improves the SCP. Adsorption is an exothermic process and the heat released should be effectively removed, since the adsorption capacity decreases at higher temperatures. Incorporation of additional fins enhances the heat transfer and the reactor is maintained at lower temperature, resulting in higher SCP.

On the other hand, increasing the size of the heat exchanger affects negatively the COP. During the desorption phase an amount of thermal energy should be provided to the packed bed, in order to increase its temperature and pressure, leading to the desorption of the adsorbate. To achieve this, the heat exchanger

solid should be heated as well, and this energy is lost in every cycle. Therefore, increasing the size of the heat exchanger increases the additional thermal energy input to the system and thus, it decreases the COP.

Consequently, a conflict arises with respect to the solid mass of the heat exchanger. The design strategy should ensure enhanced heat transfer inside the packed bed, while using the minimum amount of additional mass in the heat exchanger.

Reliable computational distributed-parameter models can contribute substantially to the design of the adsorption reactors. If they are proved to predict the performance of the system with an acceptable accuracy, they allow to conduct numerous computational simulations in a shorter period of time, with less effort and lower cost than actual experiments. Furthermore, they provide temporospatial information of all the physical quantities within the domain, even those that are impossible to measure experimentally. In this sense, they allow us to improve our understanding of the physical phenomena involved.

Within this context, several distributed-parameter models were presented in the peer-reviewed literature. A summary of the most important aspects of these models is presented in Table 1 and it is discussed later in this section.

The scope of the presented models is diverse. Some models were used in order to study the validity of various modelling strategies. Mhimid [10] investigated the validity of the local thermal equilibrium assumption, in comparison to the local thermal nonequilibrium approach. Ilis et al. [11] performed an analysis regarding the applicability of the isobaric assumption inside the packed bed, by comparing the non-uniform and the uniform pressure approach. Chahbani et al. [12] used a numerical model to study and compare the effect of different modelling strategies with respect to the intraparticle mass transfer kinetics.

Other works were dedicated to the experimental validation of the model. Zhao et al. [13, 14] constructed a numerical model for the simulation of the adsorption refrigeration tube and conducted experimental studies for the validation of the model. Similarly, Zhang and Wang [15] and Jribi et al. [16] performed the same task for a tubular reactor with axial and radial fins, respectively. Luo and Tondeur [17] and Wu et al. [18] conducted experimental studies on annular adsorption reactors, in order to validate numerical models for adsorption refrigerators and adsorption-based desalination processes, respectively.

Distributed-parameter models were also used to evaluate the system performance when employing different adsorption materials. Saha et al. [19] used a distributed-parameter model to compare the performance of an adsorption chiller based on two different adsorbent materials, silica gel RD and the composite sorbent SWS-1L. Sun et al. [20] studied the performance of an adsorption reactor using zeolite 13X as an adsorbent and compared the utilization of two adsorbates, water and ammonia.

Another research direction using distributed-parameter models is to investigate the performance of the system under different operational conditions and recovery strategies. Chua et al. [21] studied the effect of the heat recovery strategy and the effect of the cycle time on the COP and the cooling capacity. They also compared results obtained by distributed-parameter and lumped-parameter models, concluding that

the latter underpredicts the performance of the system. Leong and Liu [22] numerically investigated the incorporation of heat and mass recovery strategies on a tubular reactor without fins. Pan et al. [23] used a distributed-parameter model to study and compare three different heat recovery strategies on a tubular reactor with radial fins. Hong et al. [24] studied the effect of several parameters, concluding that the driving heat source temperature has the strongest influence on the SCP. Solmuş et al. [25] studied the influence of operational parameters such as the condenser and evaporator pressures, as well as the driving heat source and cooling temperatures. Demir [26] studied an adsorption heat pump incorporating microwave heating and compared it to the conventional approach.

Several authors used distributed-parameter models in order to investigate and improve the geometrical configuration of adsorption reactors. Niazmand and Dabzadeh [27] studied the influence of fin pitch and fin length on the performance of a tubular reactor with circular radial fins, while Mahdavikhah and Niazmand [28] studied the impact of these geometrical parameters on the performance of a tubular reactor with square radial fins. Mohammed et al. [29] proposed a reactor design consisting of two layers of packed beads separated by a vapor passage and numerically studied the impact of the particle diameter, bed thickness and thermal conductivity on the SCP. Ramji et al. [30] presented a parametric study with the objective to investigate the effect of the wall thickness on the performance of an adsorption air-conditioning system driven by exhaust heat. Kowsari et al. [31] investigated the geometrical configuration of the trapezoidal finned flat-tube heat exchanger and proposed a design procedure for reactors of this type.

Table 1 presents an extensive, though not exhaustive, summary of the distributed-parameter models published in the peer-reviewed literature [10–36]. For conciseness, numerical models used by the same research group and appear multiple times in the literature are listed only once. Simulation models related to adsorption packed bed reactors which are embedded in the solar collector such as [37, 38] are not included in the summary, as they are specific to solar energy source, as well as to ice production applications. Since numerical models are easily adaptable to other adsorption pairs, the adsorption pair and isotherm are not included in the presented summary. It should be noted that the adsorption packed bed reactors are used throughout a wide spectrum of industrial and environmental applications. Examples include gas storage (hydrogen [39], methane [40], carbon dioxide [41]), gas separation [42], carbon capture [43] and water treatment and purification [44]. Although the presented model is extensible to these applications, Table 1 is limited to numerical studies related to adsorption cooling, desalination and heat storage.

Table 1 summarizes the most important features related to the reliability, extensibility and complexity of the models. The features summarized in Table 1 are discussed below with the intention to reveal some common tendencies, important distinctions and limitations of the current state-of-the-art regarding the numerical modelling of adsorption packed bed reactors.

The experimental validation is categorized between local and global. Global experimental validation is performed at component level, based on experimental information outside the packed bed, such as the

temporal evolution of the outlet temperature of the HTF, the exterior wall temperature of the packed bed and the overall adsorption uptake. Local experimental validation is based on experimental information within the packed bed, in particular, the temporal evolution of the temperature on 3-4 different points inside the packed bed. The local experimental validation is considered more rigorous since it challenges the distributed-parameter nature of the models and therefore it increases their reliability for design purposes. The majority of the experimentally validated models are based on the global approach, while only few models are validated based on the local approach. One third of the presented numerical models are not experimentally validated, hence they are less applicable to studies aiming quantitatively accurate results.

The models are also characterized by whether they solve numerically the solid heat exchanger. When the solid is not taken explicitly into account the influence of its shape, size as well as its thermal properties cannot be appreciated and the model may be used to study only the packed bed using fixed boundary conditions. When the solid is numerically solved, the conjugate heat transfer is solved and the influence of the heat exchanger can be evaluated and improved.

The spatial discretization of the domain is also a significant factor regarding the applicability of the model. From Table 1, it can be observed that the majority of the models are based on cylindrical coordinates, hence they are restricted to reactor geometries of cylindrical shape. Structured meshes are subjected to geometric limitations with respect to the simulated geometry, whereas unstructured meshes can be used in order to simulate any potential geometry. Furthermore, unstructured meshes allow higher flexibility over the mesh density distribution, which can be adapted spatially to the physical phenomena involved.

The dimensionality of a model represents its capacity to be applied independently to the presence of geometric symmetry or symmetry of the boundary conditions. The applicability of one-dimensional and two-dimensional models depends on the presence of such symmetries, while three-dimensional models can be applied in any case. Only few of the presented models are three-dimensional, whereas the majority are either one-dimensional or two-dimensional.

Table 1 also summarizes the geometry of the packed bed reactor that was studied by the referenced models. As observed, all listed studies are dedicated to one geometry each. Tubular reactor is noted for cylindrical reactors where the HTF passes through its center and the vapor enters the packed bed from its exterior. Annular reactor is noted when the HTF passes through the exterior of the cylinder and the vapor enters through its center. The presence of fins and their type is also reported.

The vast majority of the reported distributed-parameter models use the Linear Driving Force (LDF) model to describe the intraparticle mass transfer resistance. A few models use the equilibrium approach, which neglects the adsorption kinetics, assuming local equilibrium between the gas and solid phase of the bed. The solid diffusion model (SD, or Fickian diffusion model) is generally considered to be the most accurate [24], however its computational cost is much higher. While the LDF model assumes lumped temperature and adsorption capacity over the entire adsorbent particle, the SD model requires spatial discretization

7

of the particle and numerical solution of the heat transfer and adsorbate diffusion within the adsorbent. This applies for each control volume of the mesh, increasing significantly the computational cost of the simulations, especially in three-dimensional cases. Moreover, the spatial discretization at the particle level decreases the acceptable timestep. Chabani et al. [12] compared the three approaches and concluded that outside their validity range, the LDF model underestimates the system performance and the equilibrium approach overestimates it, with respect to the diffusion model.

Regarding the interparticle mass transfer resistance, some studies assume uniform pressure throughout the packed bed [12, 33]. This isobaric assumption is not valid in the case of large packed beds or small adsorbent particle size [11], where pressure gradients are considerable. The most common approach is to use momentum equations for porous media such as the Darcy equation, the Ergun equation and the Darcy-Brinkmann equation. Authors who used commercial CFD software report using the 'classic Navier-Stokes equations' [30], Navier-Stokes equations with a sink term in the momentum equation [16] and turbulence $k - \epsilon$ model [23].

With respect to the heat transfer within the packed bed, two approaches are encountered in the literature; the most commonly used is the Local Thermal Equilibrium (LTE), while few works use the Local Thermal Nonequilibrium (LTNE, or non-local thermal equilibrium) [10, 14, 25, 35]. The LTE approach assumes that the gas and solid phases have the same temperature, therefore one energy equation is solved. This approach requires the use of effective thermal conductivity and effective specific heat capacity, assuming that the heat transfer resistance between the two phases is negligible. The LTNE approach distinguishes the temperature of the two phases, and therefore, two energy equations are solved. Each energy equation has a source term for the heat transfer between the two phases. Mhimid [10] compared the two approaches for the desorption phase. Although no significant difference was found on the total desorbed mass between the two approaches, he concluded that the LTE is not valid throughout the entire domain. Using the LTNE approach, he observed temperature differences up to $10\,^\circ\text{C}$ between gas and solid. Furthermore, the conclusion of the small discrepancy between the desorbed mass calculated by the two approaches is specific to the particularities of the studied case (geometry, dimensions, adsorption pair, desorption phase etc.) and cannot be generalized.

Based on the above discussion and with an overview of the Table 1, it becomes clear that there is a great interest for the numerical modelling of adsorption reactors. However, the previously reported models have significant limitations with respect to the simulated reactor geometry. The majority is limited only to cylindrical geometries. Moreover, only few reported models are three-dimensional, whereas the rest depend on the presence of symmetries. Furthermore, most of the reported models are either not experimentally validated, or their experimental validation is performed at component level, and thus, the distributed-parameter nature of the model is not challenged. In addition, many reported models simulate only the packed bed and they do not explicitly solve the heat exchanger, thus, they cannot be used for the study

and the improvement of the reactor performance. The literature review also reveals the absence of any comparative parametric study between different adsorption reactor geometries.

In this study, a generalized three-dimensional computational model is presented, capable to simulate any potential reactor geometry. The model exhibits reasonably good agreement against experimental results, with respect to the temporal evolution of the temperature at four point inside the packed bed reactor [16]. Both the packed bed and the solid heat exchanger domains are simulated in a dynamic conjugate manner (Figure 1(a)), thus allowing to study the influence of the latter on the reactor performance. The interaction of the two domains was carried out using the NEST platform, an in-house C++ object-oriented tool for the conjugate simulation of models of arbitrary complexity [45]. The intraparticle and interparticle mass transfer resistance were modeled using the LDF model and the Ergun equation, respectively. The heat transfer within the packed was modeled by the LTNE approach, thus two energy equations were solved. The spatial discretization of the governing equations was implemented onto three-dimensional unstructured meshes (Figure 1(b)). Versatility is provided regarding the adsorption pair and the material of the heat exchanger. The computations can be distributed in various CPUs (Figure 1(c)). Parallel computing allows the simulation of relatively large domains in reasonable computational time. The numerical model is implemented within TermoFluids, an in-house Computational Fluid Dynamics (CFD) code based on C++ programming language [46]. Coding the model rather than using commercial software provides the freedom to fully define the problem mathematically, as well as to implement numerical algorithms that assure stability and accuracy at the lowest possible computational cost.

Following the model definition, a parametric analysis is presented for five reactor geometries, with respect to their fin thickness, fin length and solid volume fraction. Furthermore, the influence of the spatial distribution of the adsorbed mass on the desorption phase is investigated. Finally, copper and aluminium are compared as heat exchanger materials and a sensitivity analysis is presented with respect to the heat transfer coefficient between the packed bed and the heat exchanger. The presented numerical model can contribute to the improvement of the design of adsorption packed bed reactors.
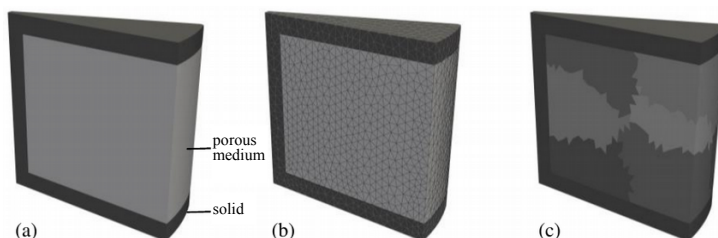

Figure 1: Conceptual images of the work process (a) geometry definition, (b) domain discretization, (c) partition on 8 CPUs for parallel computing

Table 1: Summary of distributed-parameter models used in the context of adsorption cooling, thermochemical storage and desalination

Reference	Year	Experimental validation	Solid Solution	Spatial discretization	Dim.	Reactor geometry	Intraparticle mass transfer resistance	Interparticle mass transfer resistance	Heat transfer approach
L.M. Sun et al. [20]	1995	None	Yes	Cylindrical	1d	Tubular	Equilibrium	Ergun	LTE
A. Mhimid [10]	1998	Global	No	Cylindrical	2d	Annular	LDF	Darcy	Both
L.Z. Zhang [15]	1999	Local	Yes	Cylindrical	3d	Tubular (axial fins)	LDF	Darcy	LTE
L. Luo [17]	2000	Local	No	Cylindrical	1d	Annular	Equilibrium	Diffusion	LTE
M.H. Chabani [12]	2002	None	Yes	Cylindrical	1d	Annular	Equil/LDF/SD	Isobaric	LTE
L. Marletta [32]	2002	None	Yes	Cylindrical	2d	Tubular (coated)	Equilibrium	Ergun	LTE
H.T. Chua [21]	2004	Global	Yes	Cylindrical	2d	Tubular (radial fins)	LDF	N/A	LTE
K.C. Leong [22]	2004	None	Yes	Cylindrical	2d	Tubular	LDF	Darcy	LTE
E. Voyiatzis [33]	2008	None	Yes	Cylindrical	1d	Tubular	LDF	Isobaric	LTE
W.D. Wu [34]	2009	Global	Yes	Cylindrical	2d	Annular ads. tube	LDF	Darcy	LTE
B.B. Saha [19]	2009	Global	Yes	Cylindrical	2d	Tubular (radial fins)	LDF	N/A	LTE
F.B. Cortés [35]	2009	Global	No	Cylindrical	1d	Annular	LDF	Darcy	LTNE
H. Niazmand [27]	2012	Global	Yes	Cylindrical	2d	Tubular (radial fins)	LDF	Ergun	LTE
Y.L. Zhao [13]	2012	Local	No	Cylindrical	1d	Annular ads. tube	Equilibrium	Diffusion	LTE
Y.L. Zhao [14]	2012	Local	No	Cylindrical	1d	Annular ads. tube	LDF	Darcy	LTNE
G.G. Ilis [11]	2013	None	No	Cylindrical	1d	Annular	LDF	Isobaric/Darcy	LTE
M. Mahdavikhah [28]	2013	Global	Yes	Structured Non-orthogonal	3d	Tubular (square radial fins)	LDF	Darcy	LTE
H. Demir [26]	2013	None	No	Cylindrical	1d	Annular	LDF	Darcy	LTE
M. Duquesne [36]	2014	Global	No	Cylindrical	2d	Tubular	Equilibrium	Darcy	LTE
J.W. Wu [18]	2014	Local	No	Cylindrical	1d	Annular	LDF	Darcy	LTE
H.R. Ramji [30]*	2014	Global	No	N/A	N/A	Tubular (axial fins)	LDF	Navier Stokes	LTE
S.W. Hong [24]*	2015	Global	Yes	Cylindrical	2d	Tubular (radial fins)	SD	Diffusion	LTE
İ.Solmuş [25]	2015	None	No	Cylindrical	2d	Annular	LDF	Darcy	LTNE
Q.W. Pan [23]*	2015	None	Yes	Cylindrical	2d	Tubular (radial fins)	N/A	Navier Stokes	LTE
S. Jribi [16]*	2017	Local	Yes	N/A	2d	Tubular (radial fins)	LDF	Navier Stokes	LTE
R.Mohammed [29]	2017	Global	No	Cartesian	3d	Other	LDF	Darcy-Brinkmann	LTNE
M.M. Kowsari [31]	2018	Global	Yes	Structured Non-orthogonal	3d	Finned flat tube	LDF	Darcy	LTE

*commercial CFD software was used

2. Computational model

2.1. Introduction

The adsorption packed bed reactor consists of two domains, the packed bed (containing two phases, the solid adsorbent and the gaseous adsorbate) and the solid heat exchanger. The importance of the size and shape of the heat exchanger on the heat and mass transfer inside the packed bed is crucial. In order to capture this influence, the packed bed is simulated along with the solid heat exchanger in a dynamic conjugate manner.

The respective governing equations of the two domains are presented below. The model is based on the following common assumptions: (i) constant inlet vapor pressure and temperature to the reactor, (ii) uniform void fraction and adsorbent particle shape and size, throughout the packed bed domain, (iii) the porous medium is isotropic, hence the surface porosity of the bed is equal to its volume porosity [47], (iv) the reactor is ideally insulated, (v) the specific heat capacity of the adsorbed phase corresponds to the liquid state, (vi) the adsorbate in gaseous form behaves as an ideal gas (a validated hypothesis based on [48], see section 2.2.4) and (vii) the HTF temperature is steady across the channel, an assumption justified by the experimental results of [16] (see section 3.1).

2.2. Mathematical formulation

2.2.1. Adsorption equilibrium and kinetics

The adsorption pair considered in this study is water-silica gel type RD, manufactured by Fuji Silysia Chemical LTD. [49]. The adsorption equilibrium capacity is calculated by the Tóth isotherm, experimentally derived by Wang et al. [50] for the temperature and pressure range under consideration in this study. The Tóth isotherm is expressed by equation (1) and the relevant input parameters are listed in Table 3.

$$w^*(P,T) = \frac{K_0 \exp(\Delta H_{\mathrm{ads}}/(R_{\mathrm{g}}T))P}{\left[1 + \left(\frac{K_0}{q_m}\exp(\Delta H_{\mathrm{ads}}/(R_{\mathrm{g}}T))P\right)^{\tau}\right]^{1/\tau}} \tag{1}$$

For the adsorption kinetics, the Linear Driving Force (LDF) model is used [51]. The adsorption rate is calculated as a function of the difference between the current adsorbed mass w and the equilibrium capacity w^* corresponding to the current pressure and temperature. For spherical adsorbent particles, it is expressed as:

$$\frac{dw}{dt} = \frac{60D_e}{d_{\mathrm{p}}^2}(w^* - w) \tag{2}$$

D_e is the temperature-dependent effective diffusivity. It is calculated by the Arrhenius equation, based on the reference diffusivity D_0 and the activation energy E_a.

$$D_s = D_0 \exp(-E_a/(RT)) \tag{3}$$

11

2.2.2. Mass conservation equation

The mass conservation equation describes the temporal evolution of the spatial distribution of vapor density in the reactor bed, as a result of vapor movement and sorption phenomena.

$$\epsilon_{\mathrm{b}}\frac{\partial \rho_{\mathrm{g}}}{\partial t} + \nabla \cdot (\rho_{\mathrm{g}}\vec{u}) + \rho_{\mathrm{s}}(1-\epsilon_{\mathrm{t}})\frac{\partial w}{\partial t} = 0 \tag{4}$$

where ϵ_{t} stands for total void fraction, calculated as [21]:

$$\epsilon_{\mathrm{t}} = \epsilon_{\mathrm{b}} + (1-\epsilon_{\mathrm{b}})\epsilon_{\mathrm{p}} \tag{5}$$

2.2.3. Energy conservation equations

Packed bed reactor domain. For the heat transfer inside the packed bed, the local thermal nonequilibrium approach is adopted (LTNE). Therefore, a distinct energy equation is solved for each phase. The solid energy equation describes the temporal evolution of its temperature as a function of the heat diffusion, the heat generated or consumed depending on whether adsorption or desorption is taking place and the heat exchanged with the gas phase. The gas energy equation describes the temporal evolution of its temperature as a function of heat convection, diffusion and the heat exchanged with the solid phase.

$$\text{solid: } (1-\epsilon_{\mathrm{t}})\rho_{\mathrm{s}}c_{p_{\mathrm{s}}}\frac{\partial T_{\mathrm{s}}}{\partial t} = \lambda_{\mathrm{s}}\nabla^2 T_{\mathrm{s}} + \alpha h_{\mathrm{pi}}(T_{\mathrm{g}} - T_{\mathrm{s}}) + (1-\epsilon_{\mathrm{t}})\rho_{\mathrm{s}}\Delta H_{\mathrm{ads}}\frac{\partial w}{\partial t} \tag{6}$$

$$\text{gas: } \epsilon_{\mathrm{b}}\rho_{\mathrm{g}}c_{p_{\mathrm{g}}}\frac{\partial T_{\mathrm{g}}}{\partial t} + \rho_{\mathrm{g}}c_{p_{\mathrm{g}}}\vec{u} \cdot \nabla T_{\mathrm{g}} = \lambda_{\mathrm{g}}\nabla^2 T_{\mathrm{g}} + \alpha h_{\mathrm{pi}}(T_{\mathrm{s}} - T_{\mathrm{g}}) \tag{7}$$

Parameter α is the specific exchange surface area per unit volume, which for a bed of spherical particles can be calculated as in equation (8) and h_{pi} is the adsorbent-adsorbate convective heat transfer coefficient at the particle interface which can be determined by the Nusselt number in equation (9) [10].

$$a = 6(1-\epsilon_{\mathrm{b}})/d_{\mathrm{p}} \tag{8}$$

$$\mathrm{Nu} = 2 + 1.8\mathrm{Pr}^{0.33}\mathrm{Re}^{0.5} = \frac{h_{\mathrm{pi}}d_{\mathrm{p}}}{\lambda_{\mathrm{g}}} \tag{9}$$

The influence of the adsorbed phase on the thermal capacity of the solid phase $c_{p_{\mathrm{s}}}$ is taken into account by evaluating the latter as $(c_{p_{\mathrm{s}}})_{\mathrm{dry}} + w \times c_{p_{\mathrm{l}}}$.

Solid heat exchanger domain. For the heat exchanger solid domain the heat equation is applied.

$$\rho_{\mathrm{hx}}c_{p_{\mathrm{hx}}}\frac{\partial T_{\mathrm{hx}}}{\partial t} = \lambda_{\mathrm{hx}}\nabla^2 T_{\mathrm{hx}} \tag{10}$$

2.2.4. Pressure equation

The water vapor is assumed to behave as an ideal gas, and thus, its pressure is calculated by the ideal gas law (11). The validity of this assumption has been confirmed by comparing results obtained using the ideal gas law to results obtained based on the approach proposed by the International Association for the Properties of Water and Steam (IAPWS) reported at [48]. The ideal gas law was finally used because of its considerably lower computational cost.

$$P = \rho_{\mathrm{g}} R_{\mathrm{g}} T_{\mathrm{g}} \tag{11}$$

2.2.5. Momentum equation

The momentum equation for porous media used in this study is the Ergun equation [20, 47]

$$\vec{u} + \frac{\rho_{\mathrm{g}}}{\mu} K_E \vec{u} |\vec{u}| = -\frac{K_D}{\mu} \nabla P \tag{12}$$

Where permeability K_D and Ergun inertia-related parameter K_E are calculated as:

$$K_D = \frac{d_{\mathrm{p}}^2 \epsilon_{\mathrm{b}}^3}{150(1 - \epsilon_{\mathrm{b}})^2} \text{ and } K_E = \frac{1.75 d_{\mathrm{p}}}{150(1 - \epsilon_{\mathrm{b}})} \tag{13}$$

2.2.6. Boundary conditions

In this section, the boundary conditions applied to the two domains are presented. Figure 7 illustrates the boundary conditions for each of the five geometries considered in the parametric study.

At the interface between the two domains, the heat flux is calculated using the heat transfer coefficient h_{if}, the area of the control face A_f and the temperature difference between the heat exchanger and the adsorbent $(T_{\mathrm{hx,f}} - T_{\mathrm{s,f}})$ on the control face.

$$\dot{Q}_{\mathrm{f}} = A_{\mathrm{f}} h_{\mathrm{if}} (T_{\mathrm{hx,f}} - T_{\mathrm{s,f}}) \tag{14}$$

There is some ambiguity regarding how the exchanged heat flux is distributed to the two phases of the packed bed domain [47]. In studies dedicated to experimentally derive the heat transfer coefficient, the value reported pertains to the heat transfer coefficient between the heat exchanger and the adsorbent grains (solid phase of packed bed) [52, 53]. In [53], it is hypothesized that the heat flux between the heat exchanger and the adsorbent grain takes places partially through the stagnant vapor and that the reported value for h_{if} is an apparent heat transfer coefficient. Since these reported values pertain to the heat exchange with the adsorbent grain and they appear to include the heat flux through the stagnant vapor, in this study it is assumed that the heat flux between the two domains is exchanged exclusively between the heat exchanger and the adsorbent. Neumann boundary condition is applied for the rest variables at the interface (equation 15).

$$\frac{\partial P}{\partial \mathbf{n}} = \frac{\partial T_{\mathrm{g}}}{\partial \mathbf{n}} = \frac{\partial \rho_{\mathrm{g}}}{\partial \mathbf{n}} = 0 \tag{15}$$

For the rest boundaries, typical boundary conditions of adsorption packed bed reactors are applied. At the vapor inlet, the face of the packed bed exposed to the vapor chamber, the boundary conditions of the porous medium are described by equation (16(a-c)). The thermal flux between the heat exchanger and the vapor chamber, by means of natural convection, is neglected (equation (16d)). At the interface between the heat exchanger and the heat transfer fluid, the heat transfer is calculated by equation (17). The convective heat transfer coefficient h_{HTF} can be calculated based on the geometry channel and the flow regime, as reported in [54]. Where symmetry applies, Neumann boundary condition is applied for all variables (equation (18)). It should be noted that no-slip boundary condition applies for velocity when the pressure gradient is zero.

$$P = P_{evap} \tag{16a}$$

$$\frac{\partial T_g}{\partial \mathbf{n}} = \frac{\partial T_s}{\partial \mathbf{n}} = 0 \tag{16b}$$

$$\rho_g = \frac{P}{R_g T_g} \tag{16c}$$

$$\frac{\partial T_{hx}}{\partial \mathbf{n}} = 0 \tag{16d}$$

$$\lambda_{hx} \frac{\partial T_{hx}}{\partial \mathbf{n}} = h_{HTF}(T_{HTF} - T_{hx}) \tag{17}$$

$$\frac{\partial P}{\partial \mathbf{n}} = \frac{\partial T_g}{\partial \mathbf{n}} = \frac{\partial T_s}{\partial \mathbf{n}} = \frac{\partial T_{hx}}{\partial \mathbf{n}} = \frac{\partial \rho_g}{\partial \mathbf{n}} = 0 \tag{18}$$

2.3. Numerical model

The governing equations are a set of nonlinear partial differential equations. Discretizing them in space and time allows to solve them numerically. The temporal discretization is based on an Euler implicit scheme, adopting a multi-timestep approach which allows to reduce significantly the computational cost without compromising the accuracy of the solution. The option of using an explicit scheme (lower timestep, one iteration per timestep) or an implicit scheme (higher timestep, more sub-iterations per timestep) was evaluated by preliminary studies, concluding that the computational cost is lower for the latter. The spatial discretization is based on the control volume method using unstructured meshes. Tetrahedral elements are used for the three-dimensional cases, while for the two-dimensional cases, extruded triangular elements are used and Neumann boundary conditions are applied in the extruded direction. The diffusive terms are discretized with a second order central difference scheme and the convective terms with an upwind scheme.

The energy equations are numerically solved by the Generalized Minimal Residual (GMRES) method. For the porous medium, the two energy equations are composed in one matrix in order to accelerate convergence. The equations of the porous medium related to the mass transfer (adsorption equilibrium, adsorption

kinetics, mass conservation, pressure and velocity equations) are strongly coupled and therefore they are solved together using the Gauss-Seidel method. This strategy was found to be more robust in comparison to solving the equations individually and sequentially, allowing to use higher timestep and reduce the computational cost.

Furthermore, the aforementioned strongly coupled equations require a small timestep in order to ensure a stable and accurate solution. In a conventional approach, this timestep is imposed to the rest of the equations as well. Consequently, phenomena with larger time scales are solved at a lower timestep, resulting in a significant increase of the computational cost. In this particular case, the heat transfer phenomena, expressed by the energy equations, have larger time scale in comparison to the mass transfer phenomena. Additionally, the energy equations are the most computationally intense part of the numerical solution. Solving them at the timestep imposed by the mass transfer phenomena results in a significantly higher computational time. Therefore, a multi-timestep approach is adopted. The energy equations are solved using timestep Δt, whereas the rest equations are solved at a lower sub-timestep $\Delta t_{\mathrm{sub}} = \Delta t/(\text{sub-timesteps})$. This approach was tested, and while it does not compromise the accuracy of the solution, it drastically reduces the computational cost. Indicatively, for a particular test case, the conventional approach requires a uniform timestep of $\Delta t = 10^{-5}$, while the multi-timestep approach requires $\Delta t_{\mathrm{sub}} = 10^{-5}$ and $\Delta t = 10^{-3}$. The multi-timestep approach provides almost identical results with the conventional approach (relative error 0.0007%) and it is 13 times faster. Namely, a reduction of 92.3% of the computational time is achieved, without affecting the accuracy of the solution.

The implicit algorithm requires various sub-iterations within each domain (solid heat exchanger and packed bed domain) until convergence. After each domain sub-iteration, the two domains exchange information regarding the temperature distribution on their common interface and the heat exchange between them is calculated; subsequently, they subiterate anew, until the solution of the two domains converge. Figure 2 illustrates the algorithm of the numerical procedure for the solution of one timestep.

The simulation tool allows the parallelization of the computations on various CPUs. The number of the CPUs allocated to each domain can be chosen. In this study, since the solid domain is computationally less intensive than the packed bed domain, the allocation of the CPUs was one for the solid and three or seven for the packed bed.

2.4. Verification and experimental validation of the model

The consistency of the numerical model has been tested in terms of (i) mass conservation, (ii) energy conservation, (iii) spatial mesh independence, (iv) timestep independence, as well as (v) sufficiency of the convergence criteria of the iterative procedures involved.

Furthermore, the numerical model has been validated against experimental results published in the literature. The criterion for the election of the experiment was to provide information in various points
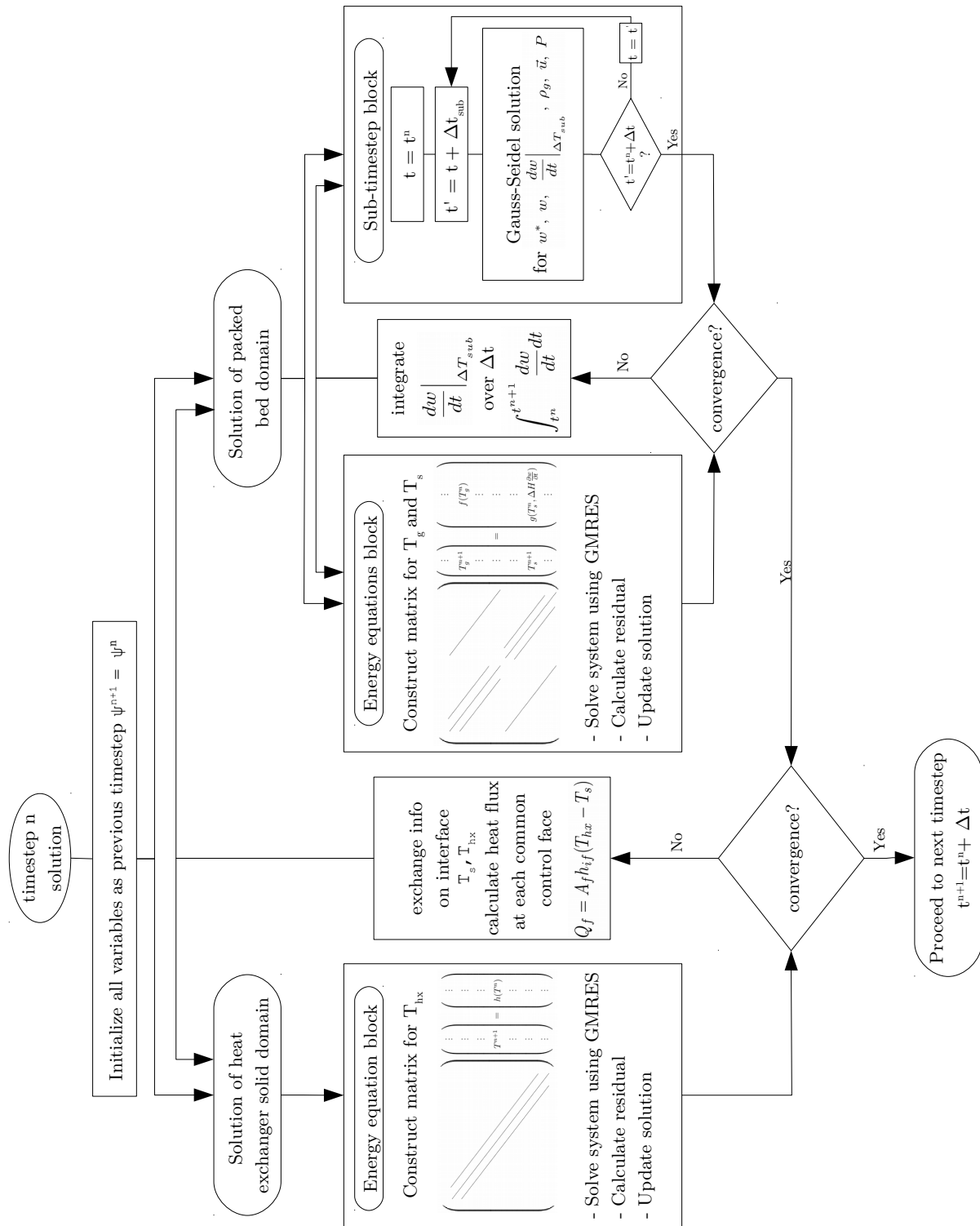
timestep n
solution

Initialize all variables as previous timestep $\psi^{n+1} = \psi^n$

Solution of packed bed domain

Solution of heat exchanger solid domain

Sub-timestep block

$t = t^n$

$t' = t + \Delta t_{sub}$

Gauss-Seidel solution
for w^*, w, $\left.\dfrac{dw}{dt}\right|_{\Delta T_{sub}}$, ρ_g, $\bar{u}$, P

$t = t'$

$t' = t^n + \Delta t$
?

No

Yes

integrate $\left.\dfrac{dw}{dt}\right|_{\Delta T_{sub}}$ over Δt

$\displaystyle\int_{t^n}^{t^{n+1}} \dfrac{dw}{dt} dt$

No

convergence?

Yes

Energy equations block

Construct matrix for T_g and T_s

$\begin{pmatrix} \ddots & \cdots & \cdots \\ \cdots & \ddots & \cdots \\ \cdots & \cdots & \ddots \end{pmatrix} \begin{pmatrix} T_g^{n+1} \\ \vdots \\ T_s^{n+1} \end{pmatrix} = \begin{pmatrix} f(T_g^n) \\ \vdots \\ g(T_s^n, \Delta H \frac{\partial w}{\partial t}) \end{pmatrix}$

- Solve system using GMRES
- Calculate residual
- Update solution

exchange info
on interface
T_s, T_{hx}
calculate heat flux
at each common
control face
$Q_f = A_f h_{if}(T_{hx} - T_s)$

No

convergence?

Yes

Energy equation block

Construct matrix for T_{hx}

$\begin{pmatrix} \ddots & \cdots & \cdots \\ \cdots & \ddots & \cdots \\ \cdots & \cdots & \ddots \end{pmatrix} T^{n+1} = \begin{pmatrix} h(T^n) \\ \vdots \\ \vdots \end{pmatrix}$

- Solve system using GMRES
- Calculate residual
- Update solution

Proceed to next timestep
$t^{n+1} = t^n + \Delta t$

Figure 2: Algorithm diagram for the numerical procedure for the solution of one timestep

16

within the packed bed (instead of information outside the packed bed), in order to achieve a rigorous experimental validation. The chosen experiment, conducted by Jribi et al.[16] satisfies this criterion, as well as it is very well documented. The experiment pertains to the adsorption of ethanol on activated carbon on a finned tubular reactor. The temperature is monitored throughout the process on four points within the packed bed, using thermocouples with an accuracy of $\pm 0.1\,\text{K}$. The thermocouples are located at 0, 1, 5 and $10\,\text{mm}$ from the tube of the reactor and they are abbreviated as T0, T1, T5 and T10. The geometry of the reactor, the position of the thermocouples as well as the calculation domain are illustrated in Figure 3.
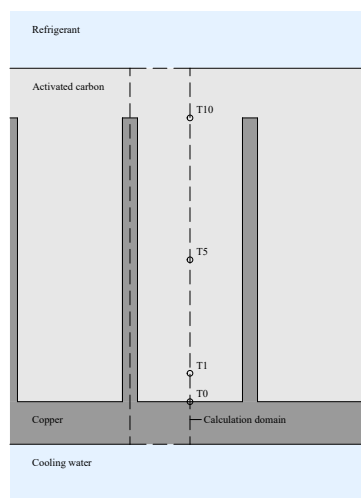
Figure 3: Schematic diagram of the geometry, calculation domain and position of thermocouples of the experiment used for validation (Reproduced image from [16])

Figure 4 shows the comparison of the temporal evolution of the temperature on those 4 points, experimentally as provided by [16] and numerically as calculated by the presented model. The model appears to capture well the temperature evolution at the positions of $1\,\text{mm}$ and $5\,\text{mm}$. At $10\,\text{mm}$, the model does not capture a significant peak. A sensitivity analysis was conducted in order to identify the model input parameters that are related to this discrepancy between the numerical and experimental results. It was detected that the temperature curves are highly sensitive to the inlet pressure profile. The authors of the experiment report the pressure profiles of the reactor and the evaporator [16]. The results presented here are based on the reactor pressure profile as inlet pressure profile. The reactor pressure profile presents a sudden peak at the moment when the reactor is connected to the evaporator and this pressure peak influences significantly the temperature peak observed at $10\,\text{mm}$. There are two uncertainties with respect to the appropriateness of this model input. First, the exact position of the reactor pressure sensor is unknown, thus it is unclear whether this profile represents the inlet pressure profile. Second, the sampling of the sensor is unknown, therefore it is possible that the aforementioned pressure peak is not captured well quantitatively. Taking

17

into account the significant influence of this input parameter along with the two uncertainties with respect to its appropriateness, the authors conjecture that this discrepancy might be attributed to an inconsistency between the experiment and the numerical simulation. At 0 mm, the general behavior is well captured, however, the model does not capture well the behavior in the period of 60 s to 90 s. At [16], it is reported that the thermocouple T0 is located at 0 mm from the solid tube, but it is unclear whether it measures the vapor temperature or if the thermocouple is in contact with the solid tube. The presented numerical results for T0 pertain to the vapor temperature. Apart from the aforementioned inconsistencies, the agreement between numerical and experimental results is considered sufficient for further utilization of the model in order to study the adsorption packed bed reactors.
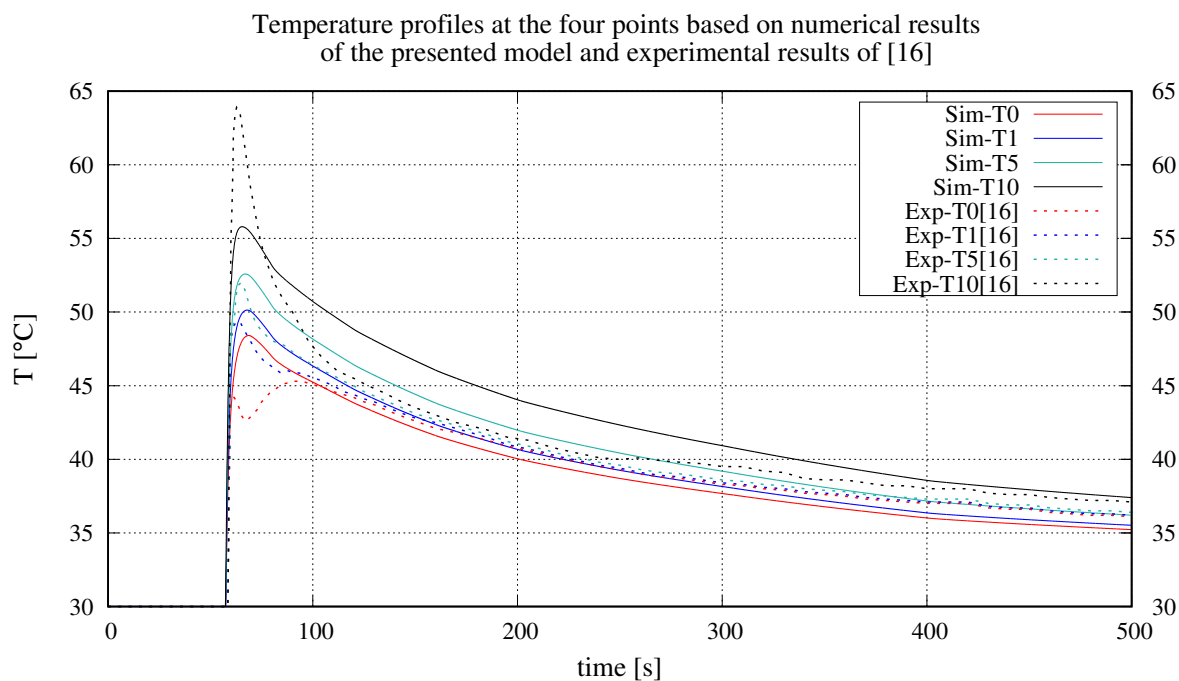
Figure 4: Comparison of the numerical results of the presented model and experimental results of [16]

3. Parametric study

3.1. Geometries under investigation

The implementation of the mathematical model on unstructured meshes provides the capability of simulating any given geometry. The objective of the parametric study is to analyze and compare the behavior of five geometries of adsorption reactors. The five geometries presented (Figure 5) are: circular channel with radial fins (GEOM-A), circular channel with square fins (GEOM-B), circular channel with axial fins

(GEOM-C), rectangular channel with corrugated fins (GEOM-D) and rectangular channel with hexagonal honeycomb fins (GEOM-E). On GEOM-A, GEOM-B, GEOM-C the HTF passes through the circular channel in the middle of the geometry. On GEOM-D, the HTF is distributed in various horizontal rectangular channels which pass above and below the metal plates with corrugated fins. On GEOM-E, the HTF passes through one vertical rectangular channel defined by the two metal plates with honeycomb fins. Taking advantage of the periodicity and symmetry of the geometries, the simulated domains are reduced as illustrated in Figure 6, in order to decrease significantly the computational cost. Figure 7 illustrates the spatial discretization and the boundary conditions (equations 15-18) for each geometry. In GEOM-A and GEOM-C, symmetries allow to reduce the problem to two-dimensional, while GEOM-B, GEOM-D and GEOM-E are three-dimensional problems.

The assumptions (iv) and (vi) of section 2.1 allow to interpret the results of the reduced geometries as representative for the entire reactor. The hypothesis of constant HTF temperature across the channel appears to be valid when observing the experimental results of [16]. During an experiment with a duration of $3800\,\mathrm{s}$, the HTF temperature difference between the inlet and the outlet of the channel (channel length $700\,\mathrm{mm}$) is higher than $1\,^{\circ}\mathrm{C}$ for less than $200\,\mathrm{s}$, with a maximum of approximately $1.8\,^{\circ}\mathrm{C}$.
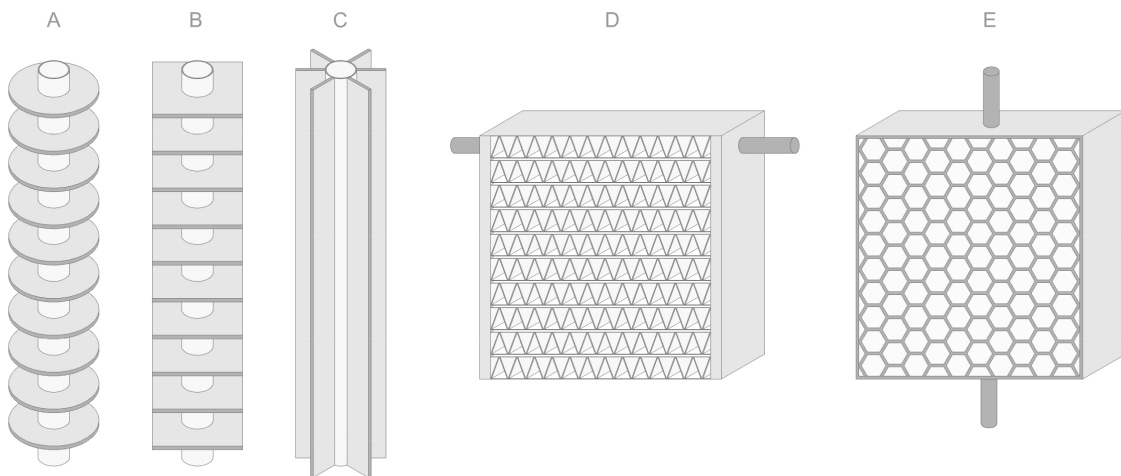
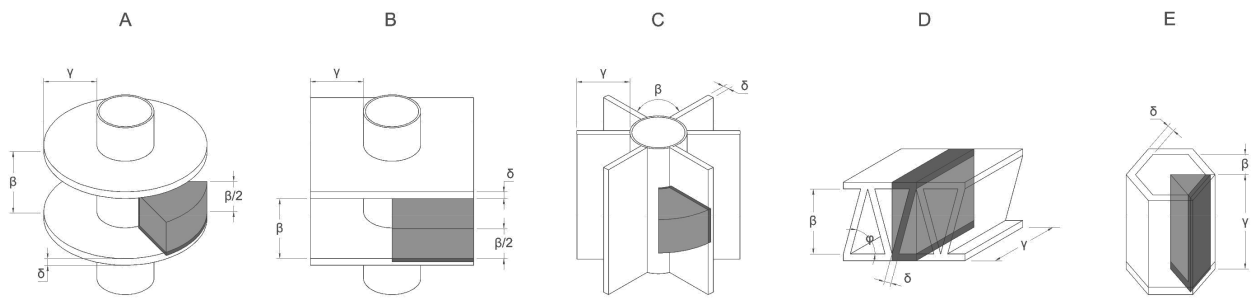Figure 5: Geometries under investigation

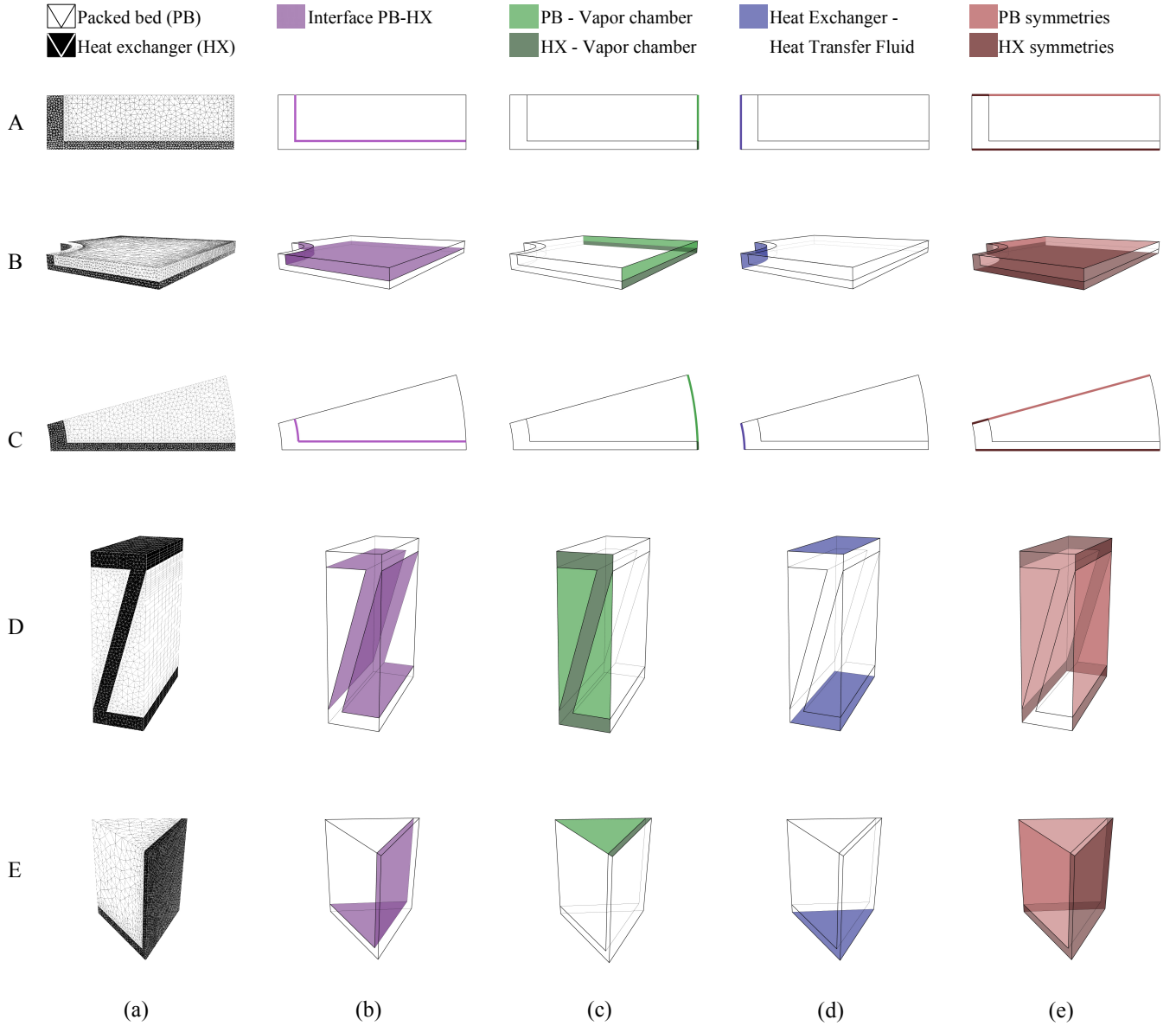Figure 6: Simulated domains taking into account the periodicity and symmetry

Figure 7: (a) Geometry discretization, (b) Interface between the two domains, (c) Face exposed to the vapor chamber for the two domains, (d) Interface between heat exchanger and heat transfer fluid and (e) Symmetry faces of the two domains

3.2. Comparability of the geometries

Apart from studying each geometry individually, it is interesting to be able to compare the performance of the proposed reactor geometries. To allow the comparison of the geometries, a set of parameters should be imposed that render the geometries comparable.

As illustrated in Figure 6, the geometries can be defined by three parameters (β, γ, δ), except GEOM-D

which requires the definition of an additional parameter, the angle ϕ, which in this study is set to $75°$.

It can be observed that two of the geometrical parameters which define each geometry are readily comparable. In this study, we call fin the mass of solid which is in contact with the HTF channel and extends inside the packed bed in order to enhance heat transfer. The two parameters that are comparable across the five geometries are the fin thickness δ and the fin length γ. The fin length is representative of the maximum distance that the vapor is required to travel inside the packed bed (from vapor inlet).

The third parameter which is designated as β in Figure 6 cannot be used for direct comparison. In the case of GEOM-A and GEOM-B, β is the fin pitch measured in distance, in GEOM-C β is the fin pitch measured as an angle, whereas for the other two geometries it is difficult to define a clearly comparable parameter. In order to fully define the geometries while maintaining their comparability, we introduce another parameter which is more meaningful regarding its impact on the performance of an adsorption cooling system. The third parameter which is imposed in order to define each geometry is the solid volume fraction, calculated as in equation (19). As explained in the Introduction, the solid mass of the heat exchanger corresponds to the additional input energy which is lost in the desorption phase of every cycle, resulting to a lower COP. When imposing the solid volume fraction, the dimension β can be calculated through the relevant geometric relations and the equation (19).

$$\text{SVF} = \frac{V_{\text{solid}}}{V_{\text{total}}} \times 100\% \tag{19}$$

3.3. Parameters under investigation

For the geometric study, a total of 65 simulations have been conducted, 13 for each geometry. The base case is for fin thickness $\delta=1\,\text{mm}$, fin length $\gamma=10\,\text{mm}$ and solid volume fraction SVF=40\%. Then, a parametric study was conducted for each of these parameters. By keeping the other two parameters steady, the solid volume fraction was studied for 20, 30, 40, 50, 60\%, the fin thickness for 0.5, 1, 2, 3, 4 mm and the fin length for 5, 10, 20, 30, 40 mm. Table 2 summarizes the reactor dimensions of the 65 simulated cases.

Table 2: Dimensions of the simulated geometries

SVF	δ	γ	β according to geometry				
[%]	[mm]	[mm]	A[mm]	B[mm]	C[°]	D[mm]	E[mm]
20	1	10	5.38	4.97	30.48	24.16	8.75
30	1	10	2.82	2.68	18.22	14.57	4.14
40	1	10	1.72	1.66	12.99	9.75	2.50
50	1	10	1.11	1.08	10.10	6.83	1.66
60	1	10	0.73	0.71	8.26	4.85	1.14
40	1	5	2.15	1.92	18.97	9.75	3.23
40	1	10	1.72	1.66	12.99	9.75	2.50
40	1	20	1.57	1.56	8.67	9.75	2.22
40	1	30	1.54	1.53	6.61	9.75	2.14
40	1	40	1.52	1.52	5.35	9.75	2.10
40	0.5	10	0.86	0.83	6.50	6.64	1.25
40	1	10	1.72	1.66	12.99	9.75	2.50
40	2	10	3.44	3.33	25.98	15.63	5.00
40	3	10	5.16	4.99	38.98	21.37	7.50
40	4	10	6.88	6.65	51.97	27.05	10.00

The geometries and the meshes were created using Ansys ICEM CFD mesh generator. Scripting tools were used, in order to automatize the mesh generation process. All meshes were imposed to mesh and timestep independence tests. The average values across the 65 meshes regarding the smallest and largest control volume of each mesh are $1.71 \times 10^{-11}\mathrm{m}^3$ and $4.76 \times 10^{-10}\mathrm{m}^3$, respectively. The number of the control volumes ranged between 625 and 10920, depending on the geometry size.

For the presented geometric study, the heat exchanger material is copper. The simulations were repeated with aluminium as heat exchanger material and the results are commented in section 4.2.4.

3.4. Simulation details

The initial conditions of the simulation assume that the adsorbent is desorbed and pre-cooled. The initial adsorbed mass corresponds to the adsorption equilibrium capacity for the condenser pressure and the heating fluid temperature of a typical cycle ($P = 4243\,\mathrm{Pa}$ and $T = 80\,^\circ\mathrm{C}$). The simulation begins when the reactor is connected to the evaporator and the adsorption process is initiated. The simulation is stopped when the relative average adsorbed mass $\overline{w}_{\mathrm{rel}}$ (equation 20) reaches 70 %, namely when the average adsorbed

23

mass of the reactor $\overline{w}$ reaches the $70\,\%$ of the difference between the initial adsorbed mass w_{init} and the adsorption equilibrium capacity w^*, which corresponds to the evaporator pressure and HTF temperature ($P = 1228\,\mathrm{Pa}$ and $T = 30\,^\circ\mathrm{C}$). The latter w^* is the adsorbed mass that would have been achieved if the process continued for a very long period. The time required for this process is denoted as $t_{70\%}$. The simulation is terminated before reaching equilibrium, since the adsorption rate becomes significantly low while approaching equilibrium (see section 4.2.2), and this regime is not interesting for practical purposes.

$$\overline{w}_{\mathrm{rel}} = \frac{\overline{w} - w_{\mathrm{init}}}{w^*\big|_{(P_{\mathrm{evap}}, T_{\mathrm{HTF}})} - w_{\mathrm{init}}} \times 100\% \tag{20}$$

Table 3 summarizes the input parameters of the numerical study. With respect to the heat transfer coefficient between the packed bed and the heat exchanger h_{if}, there are significant discrepancies across the reported values in the literature. In a recent review, Y. Aristov reported that using the Large Temperature Jump method it was revealed that the h_{if} can reach values of 100-250 $\mathrm{W\,m^{-2}\,K^{-1}}$, much higher than the commonly reported values of 15-50 $\mathrm{W\,m^{-2}\,K^{-1}}$ [55]. It should be mentioned that the value of h_{if} is often not reported. Indicatively, out of the 27 studies listed in Table 1, in 14 studies the value is not reported, while in 3 other studies the thermal resistance between the packed bed and the heat exchanger is neglected. In this study, the value of h_{if} is taken as 100 $\mathrm{W\,m^{-2}\,K^{-1}}$, which is the most conservative value from the range given at [53], where the h_{if} was experimentally derived for the Fuji silica gel type RD. A sensitivity analysis of h_{if} is presented in section 4.2.5.

Table 3: Model input parameters

Input parameter	Value	Unit	Ref.
$c_{p_{\mathrm{Al}}}$	903	$\mathrm{J\,kg^{-1}\,K^{-1}}$	[54]
$c_{p_{\mathrm{Cu}}}$	385	$\mathrm{J\,kg^{-1}\,K^{-1}}$	[54]
$c_{p_{\mathrm{s,dry}}}$	924	$\mathrm{J\,kg^{-1}\,K^{-1}}$	[50]
d_{p}	0.0005	m	
D_0	2.54×10^{-4}	$\mathrm{m^2\,s^{-1}}$	[21]
E_a	4.2×10^4	$\mathrm{J\,mol^{-1}}$	[21]
h_{if}	100	$\mathrm{W\,m^{-2}\,K^{-1}}$	[53]
K_0	7.3×10^{-13}	$\mathrm{kg_w\,kg_s\,Pa^{-1}}$	[50]
q_m	0.45	$\mathrm{kg_w\,kg_s^{-1}}$	[50]
ΔH_{ads}	2.639×10^6	$\mathrm{J\,kg^{-1}}$	[50]
ϵ_{b}	0.3955	-	[50]*
ϵ_{p}	0.4287	-	[50]*
ϵ_{t}	0.6546	-	[50]*
ρ_{s}	2027	$\mathrm{kg\,m^{-3}}$	[50]
ρ_{Al}	2702	$\mathrm{kg\,m^{-3}}$	[54]
ρ_{Cu}	8933	$\mathrm{kg\,m^{-3}}$	[54]
λ_{Al}	237	$\mathrm{W\,m^{-1}\,K^{-1}}$	[54]
λ_{Cu}	401	$\mathrm{W\,m^{-1}\,K^{-1}}$	[54]
λ_{s}	0.198	$\mathrm{W\,m^{-1}\,K^{-1}}$	[50]
τ	12	-	[50]
T_{HTF}	303.15	K	
T_{evap}	283.15	K	
P_{init}	1228	Pa	
P_{evap}	1228	Pa	
w_{init}	0.0458	$\mathrm{kg_w\,kg_s^{-1}}$	

*Calculated based on the apparent density, particle bulk density and skeletal density reported at [50]

4. Results

4.1. Evaluation parameters

The simulation results are evaluated based on the average Specific Cooling Power $[\text{W kg}_\text{s}^{-1}]$ (equation 21) and the $t_{70\%}$, as defined above. Both values are representative of the effectiveness of the reactor in terms of heat and mass transfer. Enhancing heat transfer ensures higher rate of adsorption, and therefore, higher evaporation rate and cooling production in the evaporator.

$$\text{SCP}_{\text{aver}} = \frac{\Delta m \times \Delta H_{\text{evap}}}{M_s \times t_{70\%}} = \frac{\Delta w \times \Delta H_{\text{evap}}}{t_{70\%}} \tag{21}$$

where Δm is the difference between final and initial adsorbed mass, M_s is the dry solid adsorbent mass and ΔH_{evap} is the latent heat of water evaporation.

Furthermore, the results are evaluated based on the temporal evolution of the instantaneous Specific Cooling Power, SCP_{inst}. As discussed in section 4.3, the temporal profile of the SCP_{inst} during the adsorption phase is associated with the smooth operation of the evaporator and should be taken into account during the design stage.

4.2. Results discussion

4.2.1. Average Specific Cooling Power SCP_{aver} and $t_{70\%}$

Figure 8 illustrates the effect of the solid volume fraction on the performance of the reactor, based on simulations of the five geometries for SVF 20, 30, 40, 50 and 60% ($\delta = 1\,\text{mm}$, $\gamma = 10\,\text{mm}$). The left y-axis corresponds to the SCP_{aver} and the right y-axis to the $t_{70\%}$. It should be noted that the $t_{70\%}$ axis is reversed and non-linear since $\text{SCP}_{\text{aver}} \propto \frac{1}{t_{70\%}}$. Anticipatedly, increasing the solid volume fraction of the reactor increases the SCP_{aver} and reduces $t_{70\%}$. This applies to all geometries. Since the fin thickness and length are kept identical, increasing the SVF means that the fins are more densely distributed, and therefore, the heat transfer is more effective. Consequently, the reactor is cooled more effectively and its temperature is maintained lower, resulting to higher adsorption capacity and higher SCP_{aver}. In the opposite case, for lower SVF, the fins are less densely distributed and therefore cooling the reactor is less effective, leading to higher reactor temperature and consequently to lower adsorption capacity and SCP_{aver}. Indicatively, for SVF=20%, the SCP_{aver} lies between 135.1 W/kg$_\text{s}$ (GEOM-E) and 163.6 W/kg$_\text{s}$ (GEOM-A), whereas for SVF=60%, the SCP_{aver} lies between 401.1 W/kg$_\text{s}$ (GEOM-C) and 526.9 W/kg$_\text{s}$ (GEOM-D). The time required to achieve $\overline{w}_{\text{rel}}$ of 70%, $t_{70\%}$, lies for SVF=20% between 1636.9 s (GEOM-A) and 1982.2 s (GEOM-E), whereas for SVF=60% it ranges between 508.4 s (GEOM-D) and 667.4 s (GEOM-C). It is interesting to observe that for SVF=20% the geometries have similar performance since the minimum and maximum SCP_{aver} differ by only 28.5 W/kg$_\text{s}$, while this difference for SVF=60% reaches 125.8 W/kg$_\text{s}$, demonstrating that the performance of the geometries at high SVF is significantly different. Therefore, it is observed that the solid volume fraction influences drastically the performance of the reactor.
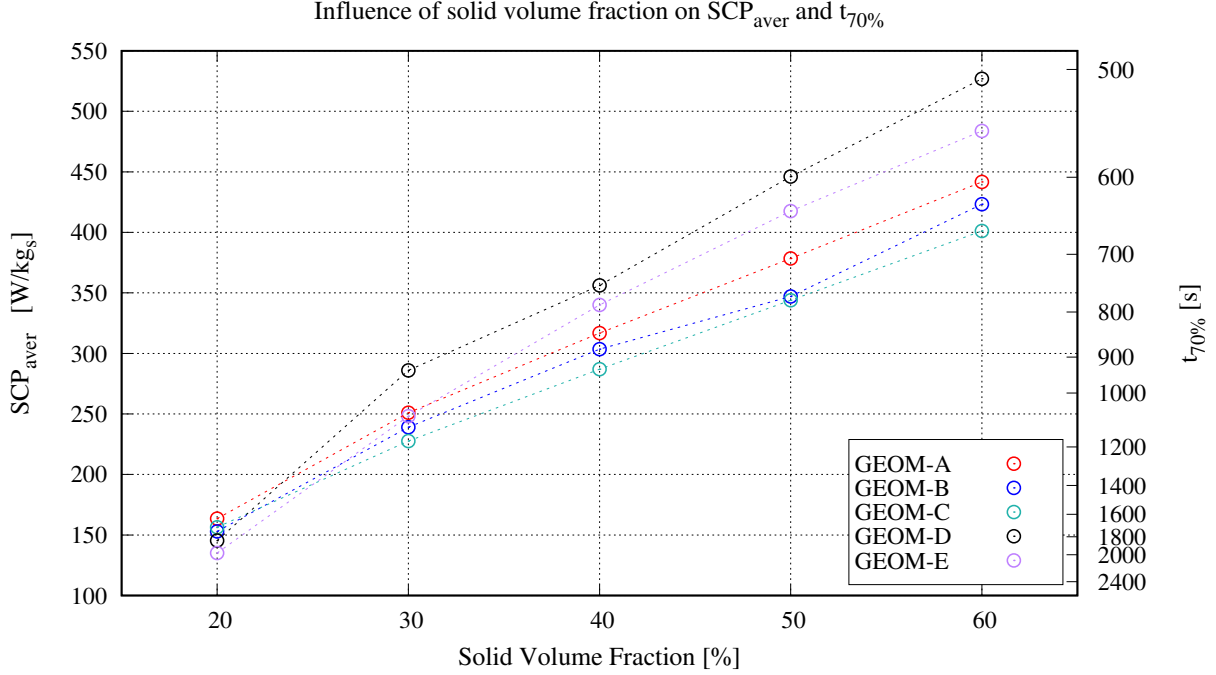
26

Figure 8: Results comparison for the influence of Solid Volume Fraction on SCP_{aver} (left y-axis) and $t_{70\%}$ (right y-axis, reversed)

Figure 9 shows the impact of the fin length on the performance of each geometry for γ values of 5, 10, 20, 30 and 40 mm ($\delta = 1\,\text{mm}$, SVF $= 40\,\%$). For the smallest fin length $\gamma = 5\,\text{mm}$, the geometries have very similar performance, since the minimum and maximum SCP_{aver} differ by only $19.0\,\text{W/kg}_s$. While for $\gamma = 5\,\text{mm}$ the performance is almost geometry-independent, for $\gamma = 40\,\text{mm}$ the SCP_{aver} ranges between $67.1\,\text{W/kg}_s$ (GEOM-C) and $257.9\,\text{W/kg}_s$ (GEOM-D), showing a strong dependence on the geometry. The performance of the reactor is expectedly lower when the fin length increases, since the packed bed volume becomes larger, and thus, the heat and mass transfer are hindered. However, it can be observed that the decrease of the reactor performance is more pronounced on the circular channel geometries (GEOM-A,B,C), with an average decrease of SCP_{aver} of approximately $80.4\,\%$ between fin length of $\gamma = 5\,\text{mm}$ and $\gamma = 40\,\text{mm}$, whereas GEOM-D and GEOM-E exhibit a decrease of $28.3\,\%$ and $49.1\,\%$, respectively.

Moreover, it is interesting to observe that the impact of the fin length variation is neither numerically constant across the studied range nor behaves in a similar manner in the five geometries. The expected performance variation as a result of γ variation is different depending on the region of the studied range, except GEOM-E, which exhibits an almost linear relation between γ and SCP_{aver}. For circular channel geometries, the gradient of the SCP_{aver} curve is much higher at the smaller fin lengths than at larger fin lengths, whereas for GEOM-D the effect is the opposite. In particular, circular channel geometries have

in average a $\left(\frac{\Delta\text{SCP}_{\text{aver}}}{\Delta\gamma}\right)$ of $-12.8\,(\text{W/kg}_{\text{s}})/\text{mm}$ for $5\,\text{mm} < \gamma < 20\,\text{mm}$, whereas for $30\,\text{mm} < \gamma < 40\,\text{mm}$ their average $\left(\frac{\Delta\text{SCP}_{\text{aver}}}{\Delta\gamma}\right)$ is $-3.7\,(\text{W/kg}_{\text{s}})/\text{mm}$. Contrarily, GEOM-D has $\left(\frac{\Delta\text{SCP}_{\text{aver}}}{\Delta\gamma}\right)$ of $-0.8\,(\text{W/kg}_{\text{s}})/\text{mm}$ for $5\,\text{mm} < \gamma < 10\,\text{mm}$ and $-3.9\,(\text{W/kg}_{\text{s}})/\text{mm}$ for $30\,\text{mm} < \gamma < 40\,\text{mm}$. To conclude, the performance of circular channel geometries become less sensitive on variations of γ at higher values of γ, while the performance of GEOM-D becomes less sensitive at lower values of γ.

Figure 10 illustrates the effect of the fin thickness for δ values of 0.5, 1, 2, 3 and 4 mm ($\gamma = 10\,\text{mm}$, SVF = 40 %). As observed in Table 2, increasing the fin thickness while maintaining the solid volume fraction steady results to geometries with greater distance between fins. The results in Figure 10 quantify the empirical notion that thinner fins densely packed are preferable to thicker fins sparsely packed. Unlike the case of fin length, there are no differences between the performance behavior of the five geometries. At $\delta = 0.5\,\text{mm}$, the SCP_{aver} ranges between $325.5\,\text{W/kg}_{\text{s}}$ (GEOM-C) and $452.1\,\text{W/kg}_{\text{s}}$ (GEOM-E), while at $\delta = 4\,\text{mm}$ it becomes less geometry-dependent, ranging between $122.5\,\text{W/kg}_{\text{s}}$ and $144.1\,\text{W/kg}_{\text{s}}$. The impact of fin thickness on SCP_{aver} ($\frac{\Delta\text{SCP}_{\text{aver}}}{\Delta\delta}$) is stronger for lower δ. For $0.5\,\text{mm} < \delta < 1\,\text{mm}$, the ($\frac{\Delta\text{SCP}_{\text{aver}}}{\Delta\delta}$) ranges between $-76.9\,(\text{W/kg}_{\text{s}})/\text{mm}$ (GEOM-C) and $-224.2\,(\text{W/kg}_{\text{s}})/\text{mm}$ (GEOM-E), while for $3\,\text{mm} < \delta < 4\,\text{mm}$ it ranges between $-27.5\,(\text{W/kg}_{\text{s}})/\text{mm}$ (GEOM-C) and $-40.1\,(\text{W/kg}_{\text{s}})/\text{mm}$ for (GEOM-D). The SCP_{aver} becomes less sensitive to fin thickness variations at higher values for δ.
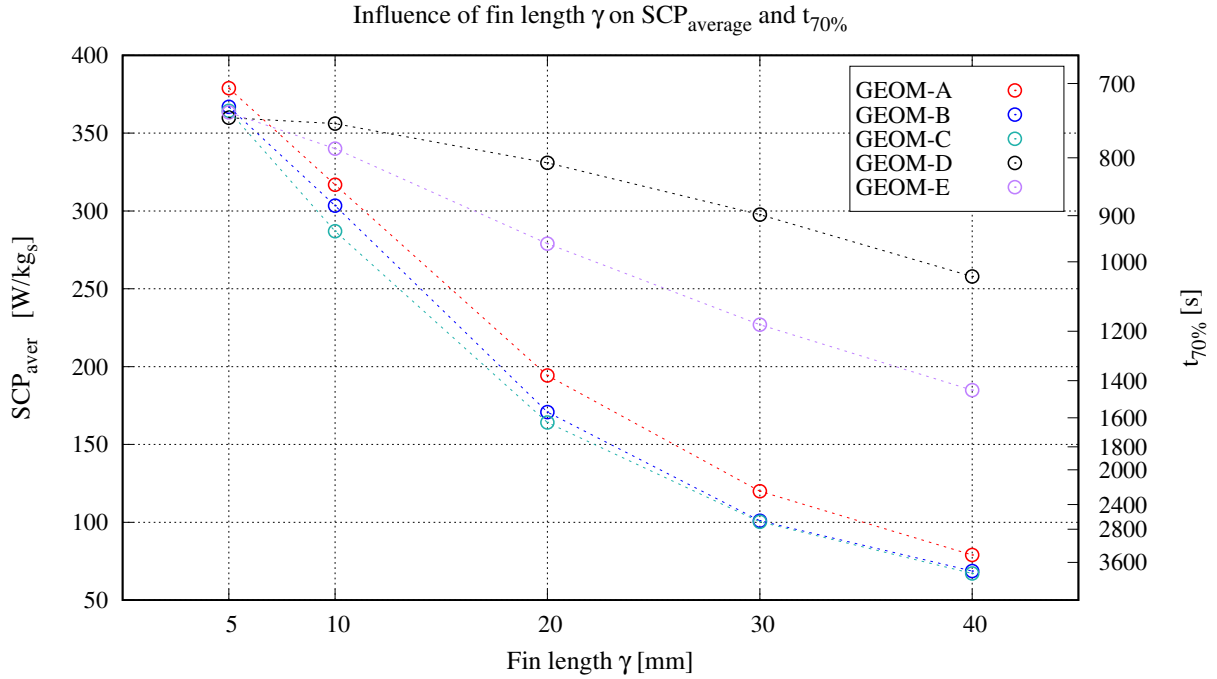

Figure 9: Results comparison for the influence of fin length on SCP_{aver} (left y-axis) and $t_{70\%}$ (right y-axis, reversed)
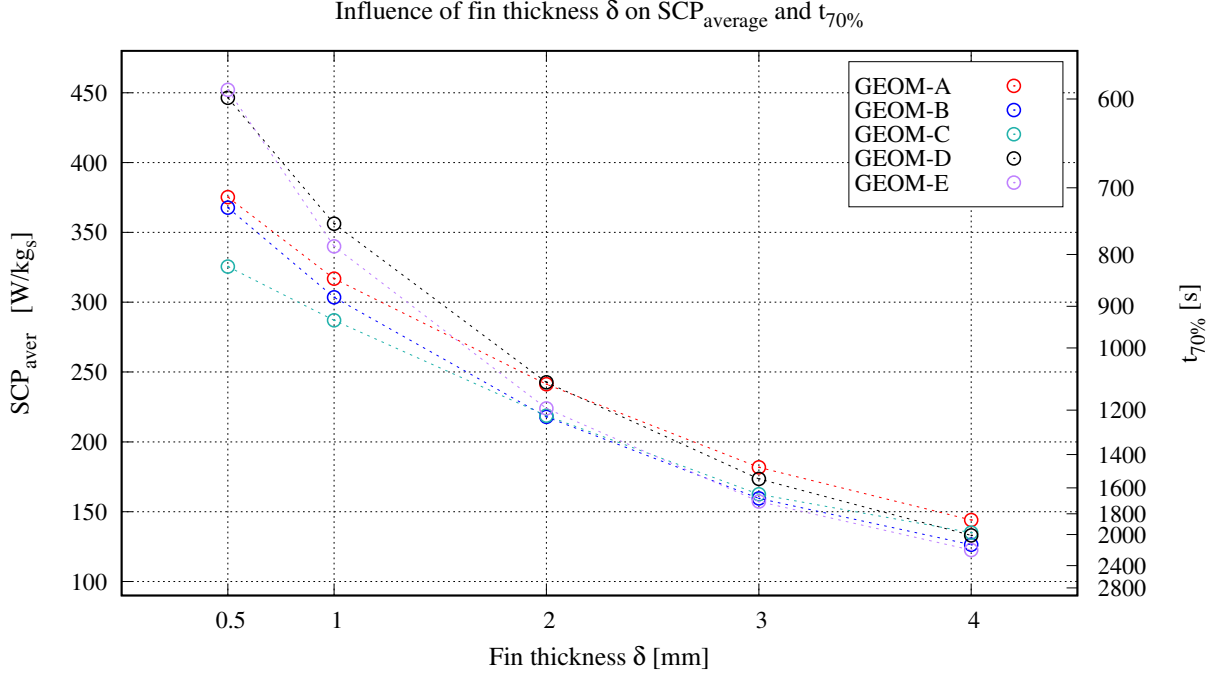
Figure 10: Results comparison for the influence of fin thickness on SCP_{aver} (left y-axis) and $t_{70\%}$ (right y-axis, reversed)

4.2.2. Instantaneous Specific Cooling Power SCP_{inst}

In the previous section, the parametric study treated the performance of the system in a macroscopic way by solely evaluating the average SCP over the course of the entire adsorption phase. In this section, the temporal evolution of the SCP_{inst} is elaborated. The SCP_{inst} is plotted against non-dimensional time $t^* = t/t_{70\%}$, for ease of comparison between different cases.

In Figure 11, the temporal evolution of SCP_{inst} for GEOM-A is shown for SVF values of 20, 30, 40, 50 and 60%. As observed, all cases exhibit a SCP_{inst} of approximately $1240\,W/kg_s$ at the beginning of the adsorption process. Then the SCP_{inst} drops rapidly for lower SVF values, while the decrease for higher SVF values is smoother. All geometries adsorb with the same rate at the beginning, and consequently, their temperature increases as a result of the exothermic nature of adsorption. For low SVF, the ineffectiveness of the heat exchanger to remove the released adsorption heat results in higher temperatures inside the reactor. Consequently, the adsorption capacity drops. On the contrary, for high SVF the heat transfer is more effective and the reactor temperature is maintained low, and therefore, its adsorption capacity is maintained high. The other geometries exhibit a similar behavior with GEOM-A, presented in Figure 11. Figure 12 compares the SCP_{inst} of the five geometries for the case of SVF=20 %. Their behavior is similar, SCP_{inst} exhibits a sudden drop at the beginning of the process and then gradually decreases. It appears that in the

29

most transient part, the SCP_{inst} of the geometries may differ by more than $100\,W/kg_s$.

Solid Volume Fraction influence on SCP_{inst} for GEOM-A (δ=1mm, γ=10mm)
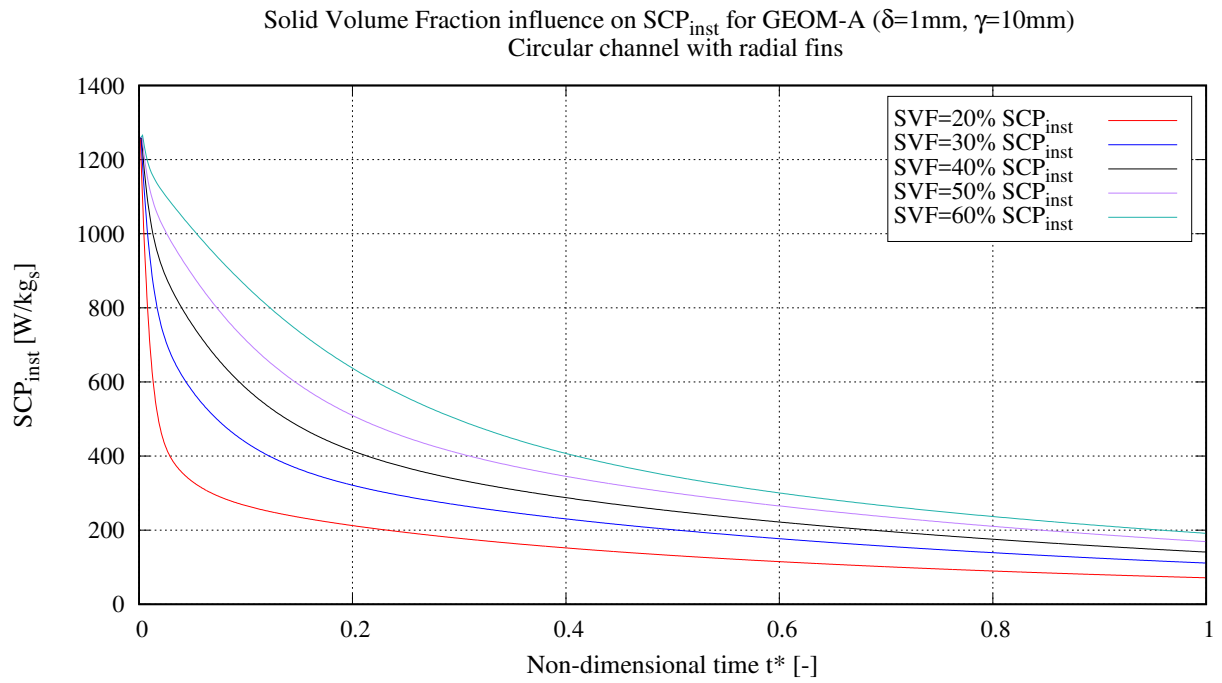Circular channel with radial fins

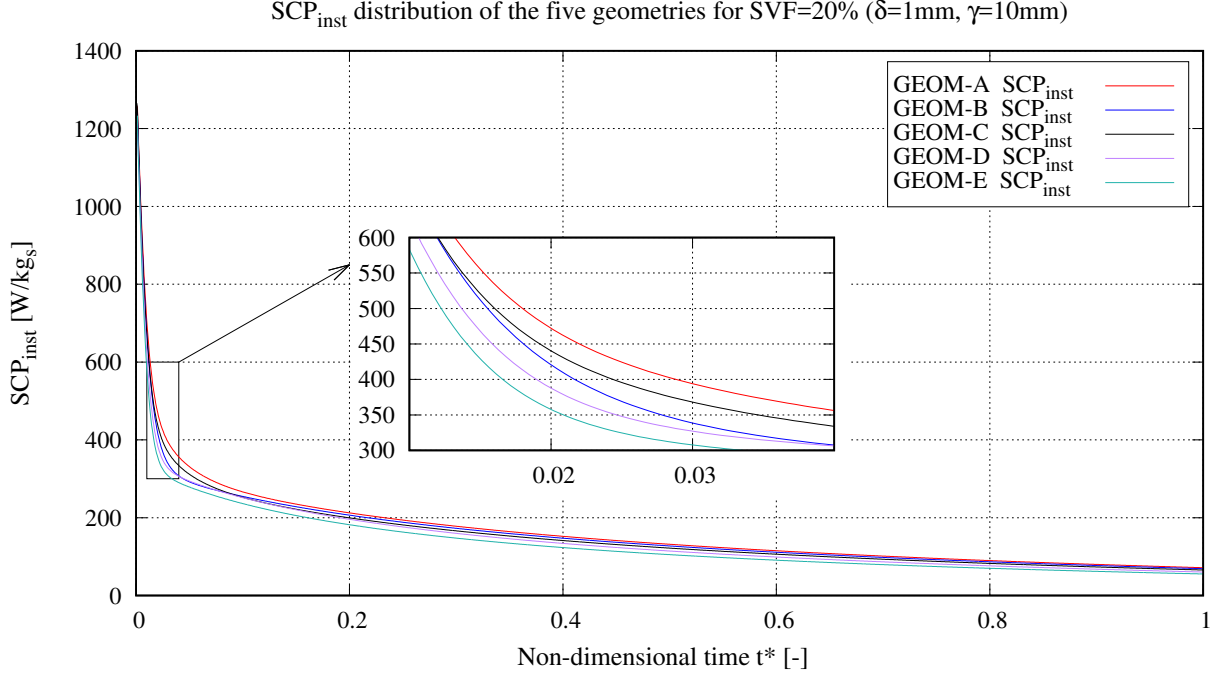Figure 11: Solid volume fraction influence on the SCP_{inst} distribution for GEOM-A

Figure 12: Comparison of the SCP_{inst} distribution of the five geometries, for the case of SVF = 20 %

Figure 13 illustrates the SCP_{inst} distribution for GEOM-C, for δ values of 0.5, 1, 2, 3 and 4 mm ($\gamma = $ 10 mm, SVF = 40 %). The same behavior is observed in the other geometries. Increasing fin thickness while maintaining the SVF steady results in thicker fins, but less densely distributed. It can be observed that while reaching equilibrium at t*=1, the SCP_{inst} for $\delta = 4$ mm is ~ 61 % lower than the SCP_{inst} for $\delta = 0.5$ mm.

Figure 14 shows the SCP_{inst} distribution for the five geometries, for the case of $\gamma = 40$ mm ($\delta = 1$ mm, SVF = 40 %). As shown earlier, the rectangular channel geometries exhibit a better performance in higher fin lengths than the circular channel geometries. It is observed that although the initial SCP_{inst} is lower for rectangular channel geometries, it does not decrease as drastically as the rest of the geometries. At t*=1, the SCP_{inst} for the rectangular channel geometries is significantly higher than for the circular channel geometries (almost triple for GEOM-E and quadruple for GEOM-D).

Figure 13: Fin thickness influence on the SCP_{inst} distribution for GEOM-B

Figure 14: Comparison of the SCP_{inst} distribution of the five geometries for the case of fin length $\gamma = 40\,\text{mm}$
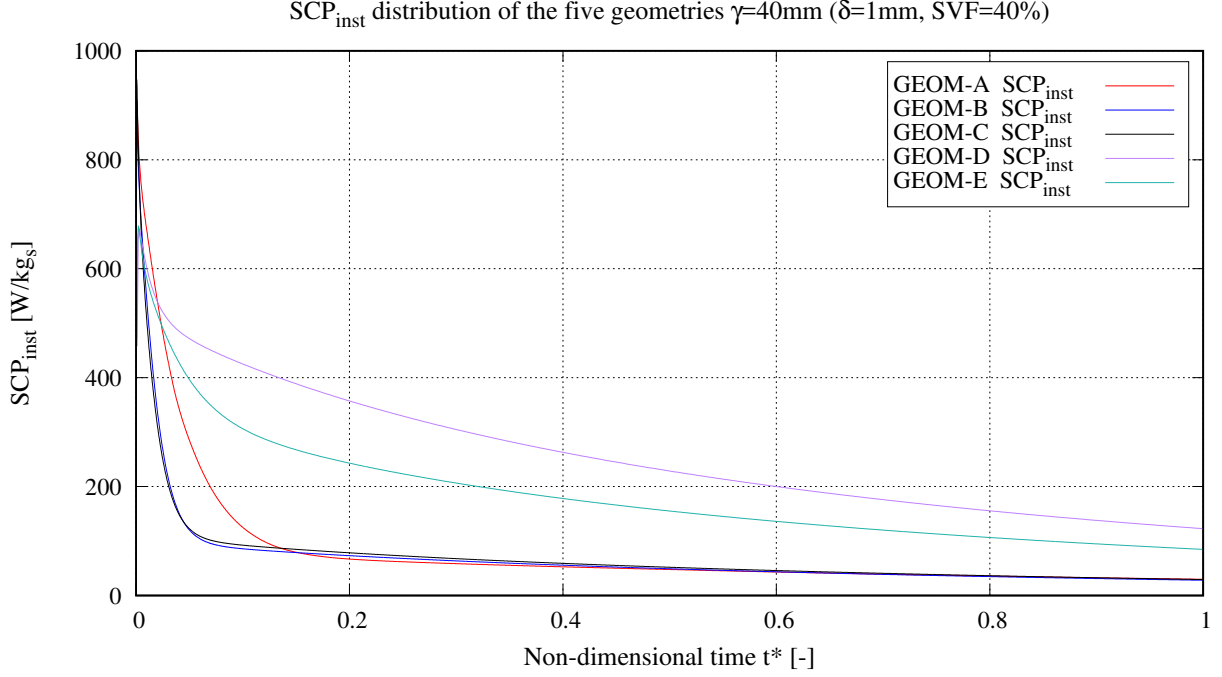
4.2.3. Spatial distribution of adsorbed mass at $t = t_{70\%}$. Influence on the desorption phase

As mentioned earlier, the simulations are terminated when the average relative adsorbed mass $\overline{w}_{rel}$ reaches 70 %. However, as observed from the results, while the average relative $\overline{w}_{rel}$ value is 70 % at $t_{70\%}$, its local values across the reactor may vary significantly. Figure 15 illustrates the spatial distribution of w_{rel} across the reactor at the end of the adsorption phase, for Solid Volume Fractions of 20, 30, 40, 50 and 60 % ($\gamma = 10\,\text{mm}$, $\delta = 1\,\text{mm}$) of GEOM-A. As observed, the distribution of w_{rel} becomes more uniform for higher SVF. The non-uniformity was quantified in terms of the range of w_{rel} and its standard deviation σ.
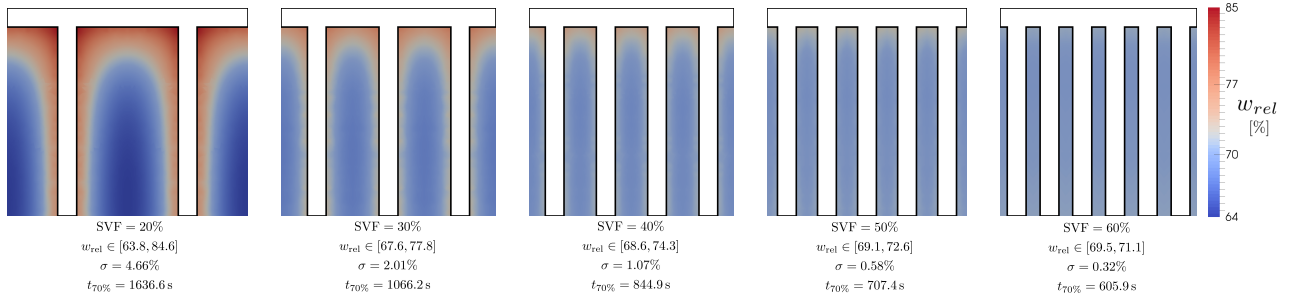

Figure 15: Spatial distribution of the w_{rel} at $t = t_{70\%}$ for different Solid Volume Fractions of GEOM-A ($\gamma = 10mm$, $\delta = 1mm$)

The spatial distribution of the adsorbed mass at the end of the adsorption phase is the initial distribution of the pre-heating phase. The objective of this section is to evaluate whether this non-uniformity affects the pre-heating and desorption phases, and consequently, the performance of the system. For this scope, the pre-heating and desorption phases were simulated for the case of GEOM-A, SVF = 20 %, $\delta = 1\,\mathrm{mm}$, $\gamma = 10\,\mathrm{mm}$.

Two cases were considered with respect to the spatial distribution of the adsorbed mass at the beginning of the pre-heating phase. In Case-I, the spatial distribution of the adsorbed mass is the final spatial distribution of the adsorption phase, as arose from the simulations; while in Case-II, a uniform spatial distribution is imposed. It should be emphasized that the global amount of adsorbed mass is the same for the two cases $\overline{w}_{\mathrm{rel}} = 70\,\%$, the only difference is its spatial distribution. The initial spatial distribution of w_{rel} is illustrated in Figure 16 for Case-I and Case-II.
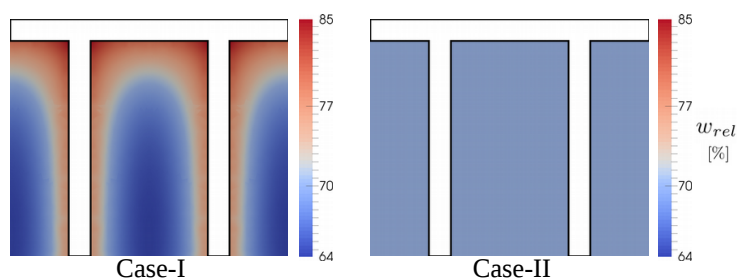

Figure 16: Initial spatial distribution of adsorbed mass at the beginning of the pre-heating phase for the two cases

At the beginning of the pre-heating phase, the reactor is disconnected from the evaporator and the HTF temperature is set to 80 °C. The reactor is heated and once its minimum pressure reaches the condenser pressure, the condenser and the reactor are connected. The initial hypothesis was that in Case-I, the desorbed vapor would be readsorbed in the regions far from the heat exchanger, which are less saturated, resulting in slower pressure increase.

However, the physical phenomena involved are more complex and their interaction is not very intuitive. In order to further understand the phenomenology, Figure 17 presents the spatial distribution of the relative adsorbed mass, sorption rate, temperature, density, pressure and velocity magnitude at $t = 40\,\mathrm{s}$ of the pre-heating phase. It should be noted that during the pre-heating phase the reactor is disconnected from the other components, thus it is a closed system and there is no mass flux at its boundaries.

The distinct difference between the two cases is that in Case-I the adsorbed mass is more accumulated in the region near the heat exchanger (Fig. 16 at $t = 0\,\mathrm{s}$ and Fig.17-a at $t = 40\,\mathrm{s}$). This results in more intense desorption in this region in comparison to Case-II (Fig.17-b), as the difference between the adsorbed mass and the new equilibrium capacity is higher, and the sorption kinetics dw/dt is proportional to $(w^* - w)$. This can be also appreciated by observing the temperature distribution (Fig.17-c). The thermal energy

provided through the heat exchanger is partly dedicated to sensible heat that increases the temperature and partly dedicated to the endothermic energy required for desorption. The temperature near the heat exchanger is lower in Case-I than in Case-II, indicating that more energy was used for desorption and less for temperature increase.

Consequently, the higher rate of desorption in Case-I results to higher density and pressure near the heat exchanger with respect to Case-II (Fig.17-d,e). The pressure gradient between the regions near and far from the heat exchanger provokes the mass flux between the two regions. Since the pressure gradient is more intense in Case-I, the vapor velocity is higher (Fig.17-f), resulting in a faster distribution of the desorbed vapor to the rest of the packed bed. Higher mass flux to the region far from the heat exchanger is associated to higher temperature increase of this region (Fig.17-c); on the one hand, because the desorbed vapor is hot, and on the other hand, because higher vapor mass is readsorbed (Fig.17-b) releasing exothermic energy. The temperature increase, along with the density increase mentioned earlier, contribute to the pressure increase in the region far from the heat exchanger, even though readsorption of vapor is more intense in Case-I than in Case-II.
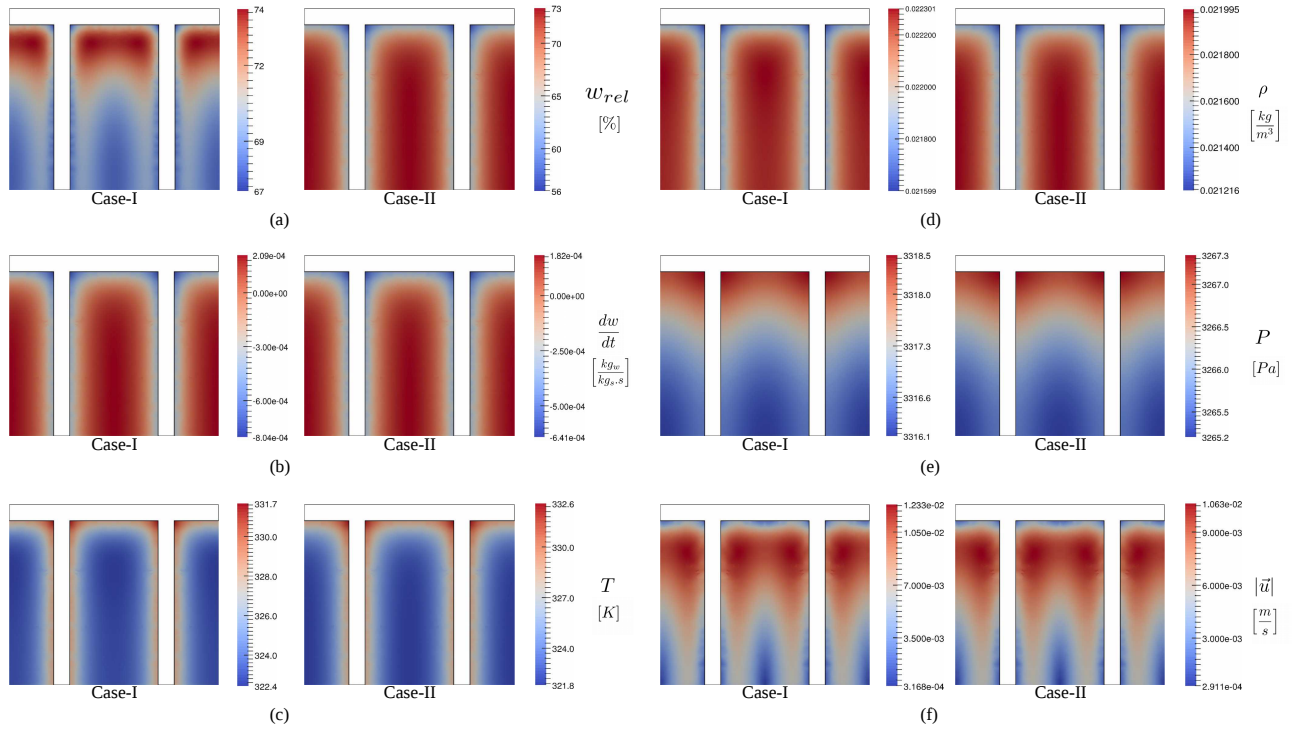

Figure 17: Spatial distribution at $t = 40\,\mathrm{s}$ of the pre-heating phase: (a) relative adsorbed mass, (b) sorption rate, (c) temperature, (d) density, (e) pressure and (f) velocity magnitude

Finally, the time required for the pre-heating phase is $50.9\,\mathrm{s}$ for Case-I and $51.8\,\mathrm{s}$ for Case-II. The total

time required for desorption (reduce $\overline{w}_{\mathrm{rel}}$ from 70 % to 20 %) is 709.6 s for Case-I and 716.8 s for Case-II. Thus, it is concluded that for the same average adsorbed mass, its spatial distribution does not affect significantly the desorption phase.

4.2.4. Heat exchanger material

The results presented above consider copper as heat exchanger material. The simulations were repeated for aluminium, in order to observe how it affects the system performance, since the properties of the two metals are quite different ($\rho_{\mathrm{Al}} = 0.3 \times \rho_{\mathrm{Cu}}$, $c_{p_{\mathrm{Al}}} = 2.3 \times c_{p_{\mathrm{Cu}}}$ and $\lambda_{\mathrm{Al}} = 0.6 \times \lambda_{\mathrm{Cu}}$). The density, the specific heat capacity and the thermal conductivity of the materials are presented in Table 3. It appears that using aluminium heat exchangers results to slightly lower $\mathrm{SCP}_{\mathrm{aver}}$ and higher $t_{70\,\%}$, since due to its lower thermal conductivity the packed bed is cooled down less effectively. However this difference is not significant and the choice of material may be based on other technoeconomic criteria. The decrease observed in $\mathrm{SCP}_{\mathrm{aver}}$ when using aluminium instead of copper does not exceed 1 %, for the studied range of SVF and fin thickness. The decrease is higher than 1 % only at higher values of fin length, $\gamma > 30\,\mathrm{mm}$, with a maximum of 3.03 % reduction for fin length $\gamma = 40\,\mathrm{mm}$ of GEOM-A.

4.2.5. Sensitivity analysis of the heat transfer coefficient h_{if}

As mentioned in section 3.4, there are significant discrepancies across the reported values of the heat transfer coefficient between the packed bed and the heat exchanger. In the results presented above, the value of $100\,\mathrm{W\,m^{-2}K^{-1}}$ was used. In this section, a series of simulations was conducted in order to evaluate the influence of this parameter. The simulations pertain to the the base case of GEOM-A (SVF = 40 %, $\gamma = 10\,\mathrm{mm}$, $\delta = 1\,\mathrm{mm}$). Figure 18 shows the $\mathrm{SCP}_{\mathrm{aver}}$ (left y-axis) and the $t_{70\%}$ (right y-axis, reversed and nonlinear) for various values of h_{if} in the range 10-350 $\mathrm{W\,m^{-2}K^{-1}}$.
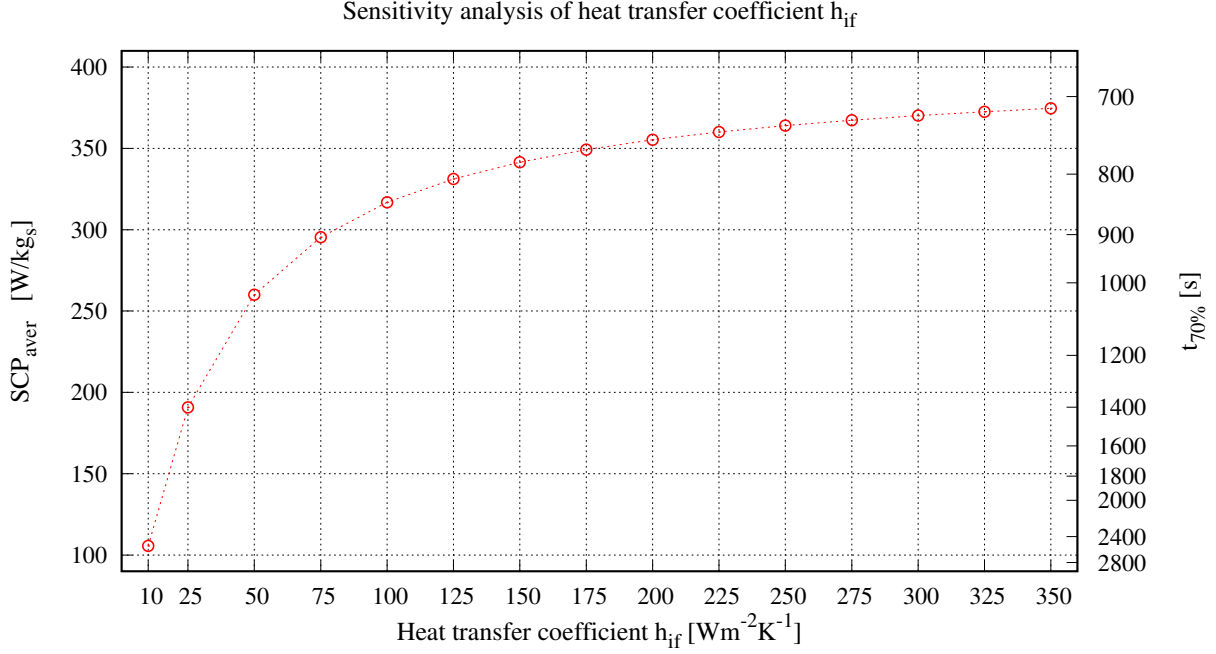
Figure 18: Influence of heat transfer coefficient h_{if} on SCP$_{aver}$ (left y-axis) and $t_{70\%}$ (right y-axis)

As observed in Figure 18, the h_{if} has a strong impact on the performance of the system. At low values of h_{if}, the heat transfer is limited by the thermal resistance between the packed bed and the heat exchanger, thus, the numerical value of h_{if} strongly affects the performance of the system. At high values of h_{if}, the performance of the system is only slightly affected by h_{if}, since the limiting factor becomes the heat transfer within the packed bed. Indicatively, the SCP$_{aver}$ for $h_{if} = 150\,\mathrm{W\,m^{-2}\,K^{-1}}$ is 3.2 times higher than the SCP$_{aver}$ for $h_{if} = 10\,\mathrm{W\,m^{-2}\,K^{-1}}$, whereas the SCP$_{aver}$ for $h_{if} = 350\,\mathrm{W\,m^{-2}\,K^{-1}}$ is 1.1 times higher than the SCP$_{aver}$ for $h_{if} = 150\,\mathrm{W\,m^{-2}\,K^{-1}}$.

4.3. Results discussion from engineering perspective

In this section, an engineering perspective is presented with respect to the results discussed in the previous sections. The SCP$_{aver}$ represents the cooling capacity of the reactor per unit mass of adsorbent. A high value of SCP$_{aver}$ is desired, since it allows to construct more compact reactors, which are associated with lower fabrication cost and higher applicability. Moreover, high SCP$_{aver}$ represents that the potential of the adsorbent material is taken advantage in larger extent, and allows to use less adsorbent mass for a given cooling capacity. Therefore, the cost-effectiveness of the reactor is improved.

As demonstrated in Section 4.2.1, the SCP$_{aver}$ increases drastically when increasing the SVF. However, as mentioned in the Introduction, increasing the SVF affects negatively the COP, since the thermal energy

input which is lost in every cycle increases. Therefore, on the one hand, in applications where the thermal energy input is not associated with additional operational costs, such as in waste heat applications, reactors with high SVF should be preferred. On the other hand, in applications of solar energy, the thermal energy input is associated with installation (solar system) and operational (auxiliary heating unit) costs. In these cases, the SVF of the reactor should be determined by evaluating both the SCP and the COP. To evaluate the effect on COP, longer simulations of the entire thermodynamic cycle are required (pre-cooling, adsorption, pre-heating, desorption). Additionally, the simulations should be performed for several cycles, until the system attains cyclic behavior and the influence of the initial conditions is eliminated. This is planned as the next stage of this study and the results presented here allow to determine the cycle period of each reactor.

With respect to the fin length, it was shown that increasing the fin length decreases the SCP of the reactor. However, the decrease of the SCP is more noticeable in the circular channel geometries, while the rectangular geometries exhibit relatively higher SCP at larger fin lengths. It is therefore recommended to prefer rectangular channel geometries when larger reactors are required. Moreover, when large amount of adsorbent must be employed, it is suggested to use various reactors of smaller fin length instead of one reactor with larger fin length. Within the studied range, the fin thickness should be as low as possible, taking into consideration the feasibility, ease and cost of fabrication.

In section 4.2.2, the temporal evolution of the SCP_{inst} was studied for the different geometries. The SCP_{inst} is representative of the cooling production, and in adsorption systems tends to have high values at the beginning of the cycle and low values while reaching equilibrium. For better operation of the evaporator, it is desired that this curve is as smooth as possible throughout the cycle. The smoothness of this curve is associated with smooth cooling production and relatively steady temperature in the evaporator. In practice, the evaporator temperature will drop at the beginning of each cycle. Disproportionally high peaks of the SCP_{inst} (as those appearing in Figure 12) enhance this temperature drop, especially in evaporators with low thermal inertia. This should be taken into account when designing the system, to evaluate the possible complications of freezing or delivering unacceptably low temperature to the cooling demand.

With respect to the heat exchanger material, the results demonstrate that for the studied range of SVF and fin thickness, copper heat exchangers perform slightly better than aluminium heat exchangers. Therefore, the choice of the material can be based on other technoeconomic criteria. The difference between the performance of the two heat exchanger materials increases at larger fin lengths. The maximum difference of SCP_{inst}, within the studied range, was found to be 3.03 % at $\gamma = 40\,\text{mm}$ of GEOM-A.

Although the study is oriented to cooling applications, the results can be usefully interpreted for other applications as well. In this study the adsorption rate is used for the calculation of the SCP, which is relevant to cooling applications. For adsorption desalination, multiplying the SCP_{aver} and SCP_{inst} by the latent heat of water evaporation ΔH_{evap}, the adsorbed mass over a cycle and the instantaneous adsorption

rate per unit mass of adsorbent can be obtained. These values allow to estimate the cyclic desalination capacity of each reactor, as well as the temporal profile of the desalination rate, which can be relevant to the evaporator design and operation parameters, such as the saline water inlet rate. For heat storage applications, multiplying the SCP_{aver} and SCP_{inst} by ΔH_{evap} and by the enthalpy of adsorption ΔH_{ads}, the released stored energy and its release rate per unit mass of adsorbent can be obtained. However, detailed studies oriented to these applications should be conducted in order to elaborate specific conclusions.

5. Conclusions

Adsorption cooling technology has significant potential environmental benefits but it remains underdeveloped due to its low performance. The design of the adsorption reactor is a crucial task for the improvement of the reactor performance. In this context, an in-house computational model is presented, capable to simulate any potential reactor geometry. The model exhibits a reasonably good agreement with experimental results. The model simulates both the packed bed and the heat exchanger, allowing to study the influence of the latter on the reactor performance. A multi-timestep approach is adopted in order to reduce drastically the computational cost.

Using the presented model, a parametric study was conducted for five reactor geometries, with respect to their solid volume fraction, fin thickness and fin length. It was demonstrated that these parameters have a strong impact on the reactor performance. Depending on the geometry, the SCP_{aver} for SVF=60 % is 2.6-3.6 times the SCP_{aver} for SVF=20 %. Similarly for the fin thickness, the SCP_{aver} for δ=0.5 mm is 2.6-3.7 times the SCP_{aver} for δ=4 mm. With respect to the fin length, a different behaviour is observed for the rectangular and the circular channel geometries. For circular channel geometries, the SCP_{aver} for γ=5 mm is 4.8-5.3 times the SCP_{aver} for γ=40 mm, whereas for rectangular channel geometries this figure is between 1.4-1.96, since they maintain relatively high SCP_{aver} at increased fin lengths. It should be noted that the intensity of the fin length influence varies throughout the studied range and behaves differently between the circular and rectangular channel geometries. Therefore, the outcome of varying the fin length should not be expected to be the same in different regions of the studied range and for different reactor geometries.

Consequently, it is recommended to use reactors with high SVF, low fin thickness and low fin length, in order to achieve high SCP_{aver}. It also suggested that if it is required to employ large amount of adsorbent mass, various reactors of small fin length should be preferred rather than one reactor with large fin length.

Furthermore, the temporal evolution of the instantaneous values of SCP are presented. Important peaks are observed at the beginning of the cycle for high values of fin length and fin thickness, as well as for low SVF values. It is strongly advised to take into consideration these peaks during the design of the evaporator, in order to avoid freezing problems or supplying unacceptably low temperature to the cooling demand

The non-uniformity of the spatial distribution of the adsorbed mass at the end of the adsorption phase

was observed and its effect on the desorption phase was investigated, concluding that it does not affect the system performance considerably.

A comparative study between two heat exchanger materials is presented. The results show that while copper is more effective than aluminium as heat exchanger material, its superiority is lower than 1% for the studied range of SVF and fin thickness. The difference between the two materials becomes appreciable at increased fin lengths, with a maximum of 3.03% at $\gamma = 40\,\mathrm{mm}$ of GEOM-A.

A sensitivity analysis was conducted with respect to the heat transfer coefficient h_{if}. The results showed that for lower values of h_{if} the performance of the system is strongly dominated by this parameter, while at higher values it affects the performance only slightly.

Lastly, the results were discussed from engineering perspective. The presented findings along with other technoeconomic criteria - such as feasibility, ease and cost of fabrication - could contribute to a beneficial design of adsorption packed bed reactors.

Acknowledgements

References

[1] International Energy Agency (IEA), World Energy Outlook 2016 (2016).

[2] M. Santamouris, On the energy impact of urban heat island and global warming on buildings, Energy Build 82 (2014) 100 − 113. `doi:10.1016/j.enbuild.2014.07.022`.

[3] United Nations, Department of Economic and Social Affairs, Population Division, World Urbanization Prospects: The 2014 Revision, Highlights (2014).

[4] Intergovernmental Panel on Climate Change, Climate Change 2014: Mitigation of Climate Change. Contribution of Working Group III to the Fifth Assessment Report of the IPCC, Cambridge University Press, Cambridge, United Kingdom and New York, NY, USA. (2014).

[5] United Nations Environment Program, Ozone Secretariat, The Montreal protocol on substances that deplete the ozone layer, New York, USA (1987).

[6] R. P. Sah, B. Choudhury, R. K. Das, A. Sur, An overview of modelling techniques employed for performance simulation of low–grade heat operated adsorption cooling systems, Renew Sustain Energy Rev 74 (2017) 364 − 376. `doi:10.1016/j.rser.2017.02.062`.

[7] M. M. Younes, I. I. El-Sharkawy, A. Kabeel, B. B. Saha, A review on adsorbent-adsorbate pairs for cooling applications, Appl Therm Eng 114 (2017) 394 − 414. `doi:10.1016/j.applthermaleng.2016.11.138`.

[8] B. Choudhury, B. B. Saha, P. K. Chatterjee, J. P. Sarkar, An overview of developments in adsorption refrigeration systems towards a sustainable way of cooling, Appl Energy 104 (2013) 554 − 567. `doi:10.1016/j.apenergy.2012.11.042`.

[9] T. Nagel, S. Beckert, C. Lehmann, R. Gläser, O. Kolditz, Multi-physical continuum models of thermochemical heat storage and transformation in porous media and powder beds—a review, Appl Energy 178 (2016) 323 − 345. `doi:10.1016/j.apenergy.2016.06.051`.

[10] A. Mhimid, Theoretical study of heat and mass transfer in a zeolite bed during water desorption: validity of local thermal equilibrium assumption, Int J Heat Mass Transf 41 (19) (1998) 2967 – 2977. `doi:10.1016/S0017-9310(98)00010-6`.

[11] G. G. Ilis, M. Mobedi, S. Ülkü, Comparison of uniform and non-uniform pressure approaches used to analyze an adsorption process in a closed type adsorbent bed, Transp Porous Med 98 (2013) 81 – 101. `doi:10.1007/s11242-013-0134-1`.

[12] M. Chahbani, J. Labidi, J. Paris, Effect of mass transfer kinetics on the performance of adsorptive heat pump systems, Appl Therm Eng 22 (1) (2002) 23 – 40. `doi:10.1016/S1359-4311(01)00067-9`.

[13] Y. Zhao, E. Hu, A. Blazewicz, A non-uniform pressure and transient boundary condition based dynamic modeling of the adsorption process of an adsorption refrigeration tube, Appl Energy 90 (1) (2012) 280 – 287. `doi:10.1016/j.apenergy.2010.12.062`.

[14] Y. Zhao, E. Hu, A. Blazewicz, Dynamic modelling of an activated carbon–methanol adsorption refrigeration tube with considerations of interfacial convection and transient pressure process, Appl Energy 95 (2012) 276 – 284. `doi:10.1016/j.apenergy.2012.02.050`.

[15] L. Zhang, L. Wang, Momentum and heat transfer in the adsorbent of a waste-heat adsorption cooling system, Energy 24 (7) (1999) 605 – 624. `doi:10.1016/S0360-5442(99)00018-3`.

[16] S. Jribi, T. Miyazaki, B. B. Saha, S. Koyama, S. Maeda, T. Maruyama, CFD simulation and experimental validation of ethanol adsorption onto activated carbon packed heat exchanger, Int J Refrig 74 (2017) 345 – 353. `doi:10.1016/j.ijrefrig.2016.10.019`.

[17] L. Luo, D. Tondeur, Transient thermal study of an adsorption refrigerating machine, Adsorption 6 (1) (2000) 93 – 104. `doi:10.1023/A:1008907518073`.

[18] J. W. Wu, M. J. Biggs, E. J. Hu, Dynamic model for the optimisation of adsorption-based desalination processes, Appl Therm Eng 66 (1) (2014) 464 – 473. `doi:10.1016/j.applthermaleng.2014.02.045`.

[19] B. B. Saha, A. Chakraborty, S. Koyama, Y. I. Aristov, A new generation cooling device employing $CaCl_2$-in-silica gel–water system, Int J Heat Mass Transf 52 (1) (2009) 516 – 524. `doi:10.1016/j.ijheatmasstransfer.2008.06.018`.

[20] L. Sun, N. B. Amar, F. Meunier, Numerical study on coupled heat and mass transfers in an absorber with external fluid heating, Heat Recov Syst CHP 15 (1) (1995) 19 – 29. `doi:10.1016/0890-4332(95)90034-9`.

[21] H. Chua, K. Ng, W. Wang, C. Yap, X. Wang, Transient modeling of a two-bed silica gel–water adsorption chiller, Int J Heat Mass Transf 47 (4) (2004) 659 – 669. `doi:10.1016/j.ijheatmasstransfer.2003.08.010`.

[22] K. Leong, Y. Liu, Numerical study of a combined heat and mass recovery adsorption cooling cycle, Int J Heat Mass Transf 47 (22) (2004) 4761 – 4770. `doi:10.1016/j.ijheatmasstransfer.2004.05.030`.

[23] Q. Pan, R. Wang, L. Wang, Comparison of different kinds of heat recoveries applied in adsorption refrigeration system, Int J Refrig 55 (2015) 37 – 48. `doi:10.1016/j.ijrefrig.2015.03.022`.

[24] S. Hong, S. Ahn, O. Kwon, J. Chung, Optimization of a fin-tube type adsorption chiller by design of experiment, Int J Refrig 49 (2015) 49 – 56. `doi:10.1016/j.ijrefrig.2014.09.022`.

[25] İsmail Solmuş, C. Yamali, C. Yildirim, K. Bilen, Transient behavior of a cylindrical adsorbent bed during the adsorption process, Appl Energy 142 (2015) 115 – 124. `doi:10.1016/j.apenergy.2014.12.080`.

[26] H. Demir, The effect of microwave regenerated adsorbent bed on the performance of an adsorption heat pump, Appl Therm Eng 50 (1) (2013) 134 – 142. `doi:10.1016/j.applthermaleng.2012.06.022`.

[27] H. Niazmand, I. Dabzadeh, Numerical simulation of heat and mass transfer in adsorbent beds with annular fins, Int J Refrig 35 (3) (2012) 581 – 593. `doi:10.1016/j.ijrefrig.2011.05.013`.

[28] M. Mahdavikhah, H. Niazmand, Effects of plate finned heat exchanger parameters on the adsorption chiller performance, Appl Therm Eng 50 (1) (2013) 939 – 949. `doi:10.1016/j.applthermaleng.2012.08.033`.

[29] R. H. Mohammed, O. Mesalhy, M. L. Elsayed, L. C. Chow, Novel compact bed design for adsorption cooling systems: Parametric numerical study, Int J Refrig 80 (2017) 238 – 251. `doi:10.1016/j.ijrefrig.2017.04.028`.

[30] H. R. Ramji, S. L. Leo, M. O. Abdullah, Parametric study and simulation of a heat-driven adsorber for air conditioning system employing activated carbon–methanol working pair, Appl Energy 113 (2014) 324 – 333. `doi:10.1016/j.apenergy.2013.07.017`.

[31] M. M. Kowsari, H. Niazmand, M. M. Tokarev, Bed configuration effects on the finned flat-tube adsorption heat exchanger performance: Numerical modeling and experimental validation, Appl Energy 213 (2018) 540 – 554. `doi:10.1016/j.apenergy.2017.11.019`.

[32] L. Marletta, G. Maggio, A. Freni, M. Ingrasciotta, G. Restuccia, A non-uniform temperature non-uniform pressure dynamic model of heat and mass transfer in compact adsorbent beds, Int J Heat Mass Transf 45 (16) (2002) 3321 – 3330. `doi:10.1016/S0017-9310(02)00045-5`.

[33] E. Voyiatzis, J. Palyvos, N.-C. Markatos, Heat-exchanger design and switching-frequency effects on the performance of a continuous type solar adsorption chiller, Appl Energy 85 (12) (2008) 1237 – 1250. `doi:10.1016/j.apenergy.2008.03.005`.

[34] W.-D. Wu, H. Zhang, D.-W. Sun, Mathematical simulation and experimental study of a modified zeolite 13X–water adsorption refrigeration module, Appl Therm Eng 29 (4) (2009) 645 – 651. `doi:10.1016/j.applthermaleng.2008.03.037`.

[35] F. B. Cortés, F. Chejne, J. M. Mejía, C. A. Londoño, Mathematical model of the sorption phenomenon of methanol in activated coal, Energy Convers Manage 50 (5) (2009) 1295 – 1303. `doi:10.1016/j.enconman.2009.01.017`.

[36] M. Duquesne, J. Toutain, A. Sempey, S. Ginestet, E. P. del Barrio, Modeling of a nonlinear thermochemical energy storage by adsorption on zeolites, Appl Therm Eng 71 (1) (2014) 469 – 480. `doi:10.1016/j.applthermaleng.2014.07.002`.

[37] M. Louajari, A. Mimet, A. Ouammi, Study of the effect of finned tube adsorber on the performance of solar driven adsorption cooling machine using activated carbon–ammonia pair, Appl Energy 88 (3) (2011) 690 – 698. `doi:10.1016/j.apenergy.2010.08.032`.

[38] G. Brites, J. Costa, V. Costa, Influence of the design parameters on the overall performance of a solar adsorption refrigerator, Renew Energy 86 (2016) 238 – 250. `doi:10.1016/j.renene.2015.07.099`.

[39] C. Corgnale, B. Hardy, R. Chahine, D. Cossement, Hydrogen desorption using honeycomb finned heat exchangers integrated in adsorbent storage systems, Appl Energy 213 (2018) 426 – 434. `doi:10.1016/j.apenergy.2018.01.003`.

[40] M. Beckner, A. Dailly, A pilot study of activated carbon and metal–organic frameworks for methane storage, Appl Energy 162 (2016) 506 – 514. `doi:10.1016/j.apenergy.2015.10.110`.

[41] N. A. Qasem, R. Ben-Mansour, M. A. Habib, An efficient CO_2 adsorptive storage using MOF-5 and MOF-177, Appl Energy 210 (2018) 317 – 326. `doi:10.1016/j.apenergy.2017.11.011`.

[42] R. Yang, Gas separation by adsorption processes, Butterworth Publishers, Boston, 1987.

[43] R. Ben-Mansour, M. Habib, O. Bamidele, M. Basha, N. Qasem, A. Peedikakkal, T. Laoui, M. Ali, Carbon capture by physical adsorption: Materials, experimental investigations and numerical modeling and simulations – a review, Appl Energy 161 (2016) 225 – 255. `doi:10.1016/j.apenergy.2015.10.011`.

[44] A. Bonilla-Petriciolet, D. Mendoza-Castillo, H. Reynel-Ávila, Adsorption processes for water treatment and purification, Springer International Publishing, 2017.

[45] J. Lopez, Parallel object-oriented algorithms for simulation of multiphysics : application to thermal systems, Ph.D. thesis, Universitat Politècnica de Catalunya (2016).

[46] O. Lehmkuhl, C. Perez-Segarra, R. Borrell, M. Soria, A. Oliva, Termofluids: A new parallel unstructured CFD code for the simulation of turbulent industrial problems on low cost PC Cluster, in: Parallel Computational Fluid Dynamics 2007, Springer Berlin Heidelberg, 2009, pp. 275–282.

[47] A. D. Nield, A. Bejan, Convection in Porous Media, 4th Edition, Springer-Verlag New York, 2013.

[48] W. Wagner, H. J. Kretzschmar, International Steam Tables - Properties of Water and Steam based on the Industrial Formulation IAPWS-IF97, 2nd Edition, Springer-Verlag Berlin Heidelberg, 2008.

[49] Fuji Silysia Chemical LTD. (Nagoya, Japan).

[50] X. Wang, W. Zimmermann, K. C. Ng, A. Chakraboty, J. U. Keller, Investigation on the isotherm of silica gel+water systems, J Therm Anal Cal 76 (2) (2004) 659 – 669. doi:10.1023/B:JTAN.0000028045.96239.7e.

[51] M. Suzuki, Adsorption Engineering, Copublished by: Kodansha, Tokyo and Elsevier Science Publishers, Amsterdam, 1990.

[52] S. Santamaria, A. Sapienza, A. Frazzica, A. Freni, I. S. Girnik, Y. I. Aristov, Water adsorption dynamics on representative pieces of real adsorbers for adsorptive chillers, Appl Energy 134 (2014) 11 – 19. doi:10.1016/j.apenergy.2014.07.053.

[53] I. Glaznev, Y. Aristov, The effect of cycle boundary conditions and adsorbent grain size on the water sorption dynamics in adsorption chillers, Int J Heat Mass Transf 53 (9) (2010) 1893 – 1898. doi:10.1016/j.ijheatmasstransfer.2009.12.069.

[54] T. Bergman, A. Lavine, F. Incropera, D. D.P, Fundamentals of Heat and Mass Transfer, 7th Edition, John Wiley and Sons, 2011.

[55] Y. I. Aristov, Adsorptive transformation and storage of renewable heat: Review of current trends in adsorption dynamics, Renew Energy 110 (2017) 105 – 114. doi:10.1016/j.renene.2016.06.055.